The Astrophysical Journal, 970:118 (31pp), 2024 August 1 https://doi.org/10.3847/1538-4357/ad4a62

A Multiwavelength, Multiepoch Monitoring Campaign of Accretion Variability in T Tauri Stars from the ODYSSEUS Survey. I. HST Far-UV and Near-UV Spectra

John Wendeborn[1], Catherine C. Espaillat[1], Sophia Lopez[1], Thanawuth Thanathibodee[1], Connor E. Robinson[2], Caeley V. Pittman[1], Nuria Calvet[3], Nicole Flors[1], Fredrick M. Walter[4], Ágnes Kóspál[5,6,7], Konstantin N. Grankin[8,19], Ignacio Mendigutía[9], Hans Moritz Günther[10], Jochen Eislöffel[11], Zhen Guo[12], Kevin France[13], Eleonora Fiorellino[14], William J. Fischer[15], Péter Ábrahám[5,6,16], and Gregory J. Herczeg[17,18]

[1] Institute for Astrophysical Research, Department of Astronomy, Boston University, 725 Commonwealth Avenue, Boston, MA 02215, USA
[2] Department of Physics & Astronomy, Amherst College, C025 Science Center, 25 East Drive, Amherst, MA 01002, USA
[3] Department of Astronomy, University of Michigan, 1085 South University Avenue, Ann Arbor, MI 48109, USA
[4] Department of Physics and Astronomy, Stony Brook University, Stony Brook, NY 11794-3800, USA
[5] Konkoly Observatory, HUN-REN Research Centre for Astronomy and Earth Sciences, CSFK, MTA Centre of Excellence, Konkoly-Thege Miklós út 15-17, Hungary
[6] ELTE Eötvös Loránd University, Institute of Physics, Pázmány Péter sétány 1/A, 1117 Budapest, Hungary
[7] Max Planck Institute for Astronomy, Königstuhl 17, 69117 Heidelberg, Germany
[8] Crimean Astrophysical Observatory, 298409 Nauchny, Republic of Crimea
[9] Centro de Asrobiología, (CSIC-INTA), Departamento de Astrofísica, ESA-ESAC Campus, E-28691 Madrid, Spain
[10] Kavli Institute for Astrophysics and Space Research, Massachusetts Institute of Technology, 77 Massachusetts Ave., Cambridge MA, 02139, USA
[11] Thüringer Landessternwarte, Sternwarte5, D-07778 Tautenburg, Germany
[12] Instituto de Física y Astronomía, Universidad de Valparaíso, ave. Gran Bretaña, 1111, Casilla 5030, Valparaíso, Chile
[13] Laboratory for Atmospheric and Space Physics, University of Colorado Boulder, Boulder, CO 80303, USA
[14] INAF-Osservatorio Astronomico di Capodimonte, via Moiariello 16, 80131 Napoli, Italy
[15] Space Telescope Science Institute, 3700 San Martin Drive, Baltimore, MD 21218, USA
[16] University of Vienna, Department of Astrophysics, Türkenschanzstr. 17, 1180, Vienna, Austria
[17] Kavli Institute for Astronomy and Astrophysics, Peking University, Beijing 100871, People's Republic of China
[18] Department of Astronomy, Peking University, Beijing 100871, People's Republic of China
Received 2024 January 23; revised 2024 April 2; accepted 2024 May 9; published 2024 July 24

Abstract

The classical T Tauri star (CTTS) stage is a critical phase of the star and planet formation process. In an effort to better understand the mass accretion processes, which can dictate future stellar evolution and planet formation, a multiepoch, multiwavelength photometric and spectroscopic monitoring campaign of four CTTSs (TW Hya, RU Lup, BP Tau, and GM Aur) was carried out in 2021 and 2022/2023 as part of the Outflows and Disks around Young Stars: Synergies for the Exploration of ULLYSES Spectra program. Here we focus on the Hubble Space Telescope (HST) UV spectra obtained by the HST Director's Discretionary Time UV Legacy Library of Young Stars as Essential Standards (ULLYSES) program. Using accretion shock modeling, we find that all targets exhibit accretion variability, varying from short increases in accretion rate by up to a factor of 3 within 48 hr to longer decreases in accretion rate by a factor of 2.5 over the course of 1 yr. This is despite the generally consistent accretion morphology within each target. Additionally, we test empirical relationships between accretion rate and UV luminosity and find stark differences, showing that these relationships should not be used to estimate the accretion rate for an individual target. Our work reinforces that future multiepoch and simultaneous multiwavelength studies are critical in our understanding of the accretion process in low-mass star formation.

Unified Astronomy Thesaurus concepts: Star formation (1569); Stellar accretion (1578); Ultraviolet spectroscopy (2284); T Tauri stars (1681)

1. Introduction

Classical T Tauri stars (CTTSs) are young (<10 Myr), low-mass (<2 $M_{\odot}$) stars that are actively accreting from a surrounding protoplanetary disk. This disk is the reservoir from which planets will form (or in some cases have already formed; e.g., Keppler et al. 2018; Haffert et al. 2019; Pérez et al. 2019; Zhou et al. 2022) and dictates much of the future evolution of the system. The process of disk-to-star mass accretion, which takes place at the star–disk boundary, typically within $\sim 10R_{\star}$, is highly energetic, emitting X-rays and UV radiation (Herbst et al. 1994; Kastner et al. 2002; Günther et al. 2007), which can have a profound impact on the disk. These effects include modifying disk chemistry, modulating the presence and distance of snowlines, inhibiting dust grain growth, annealing solid dust grains, and depleting/dispersing disk material (see reviews by Bae et al. 2022; Fischer et al. 2023; Miotello et al. 2023). As such, it is important to fully understand the accretion process in order to paint a complete picture of the star/planet formation processes.

Due to the strong magnetic fields in CTTSs (1–3 kG; Johns-Krull 2007; Donati et al. 2020), accretion occurs via magnetospheric accretion (see reviews by Bouvier et al. 2007; Hartmann et al. 2016). The magnetic field truncates the disk at some radius (the inner truncation radius, $R_{\rm in}$, typically assumed to be $5R_{\star}$),

[19] While the AAS journals adhere to and respect UN resolutions regarding the designations of territories (available at http://www.un.org/press/en), it is our policy to use the affiliations provided by our authors on published articles.

Table 1
Target Parameters

Object	R.A./Decl. (J2000)	Distance (pc)	SpT	Period (days)	M_* ($M_\odot$)	$T_{\rm eff}$ (K)	$R_\star$ ($R_\odot$)	A_V (mag)	i (deg)
TW Hya	11:01:51.905/ −34:42:17.033	$59.96^{+0.37}_{-0.11}$ (a)	K7 (b)	3.57 (c)	0.79 (d)	4060 (d)	0.93 (e)	0.00 (d)	7 (f)
RU Lup	15:56:42.311/ −37:49:15.474	$156.0^{+1.2}_{-1.1}$ (a)	K7 (g)	3.71 (h)	0.65 (i)	3950 (i)	1.83[a] (i)	0.07 (i)	16 (j)
BP Tau	04:19:15.834/ +29:06:26.927	$128.3^{+0.7}_{-0.6}$ (a)	K7 (b)	7.6 (k), 8.2 (l)	0.7 (m)	4055 (n)	1.77[a] (n)	0.51 (m)	38.2 (o)
GM Aur	04:55:10.982/ +30:21:59.574	$155.0^{+1.4}_{-2.0}$ (a)	K5 (d)	6.0 (e)	1.36 (d)	4350 (d)	2.00 (e)	0.6 (b)	53 (p)

Note.
[a] Updated with current Gaia distances.
References. (a) Gaia Collaboration et al. 2023; (b) Ingleby et al. 2013; (c) Sicilia-Aguilar et al. 2023; (d) Manara et al. 2014; (e) Robinson & Espaillat 2019 (from Manara et al. 2014 with updated Gaia distances); (f) Andrews et al. 2016; (g) Sousa et al. 2023; (h) Stempels et al. 2007; (i) Herczeg et al. 2005; (j) GRAVITY Collaboration et al. 2021; (k) Vrba et al. 1986; (l) Percy & Palaniappan 2006; (m) Gullbring et al. 1998; (n) Johns-Krull et al. 1999; (o) Zhang et al. 2023; (p) Macías et al. 2018.

where the hot plasma is bound to and travels along the magnetic field lines. Along its path, it eventually reaches supersonic, freefall velocities ($v_{\rm ff}$) until it reaches the photosphere, producing highly energetic shocks and accretion hot spots.

Simulations show that the accretion flow can vary in density (Kulkarni & Romanova 2008; Romanova et al. 2008, 2012; Zhu et al. 2023b), which affects the temperature of the resulting hot spot. Denser flows create hotter hot spots that radiate more strongly at UV wavelengths, while less dense flows (i.e., cooler hot spots) peak in the optical (Calvet & Gullbring 1998; Ingleby et al. 2013; Pittman et al. 2022). This excess UV/optical emission can be modeled, assuming that it originates from accretion columns of various energy densities (Calvet & Gullbring 1998). Such modeling (often using Hubble Space Telescope (HST) UV–optical spectra) has revealed that the accretion structure not only is time variable but also varies greatly from object to object. Some stars are dominated by large, cooler hot spots driven by low-density accretion columns, while in others the accretion is dominated by high-density columns producing small but high-temperature hot spots (Ingleby et al. 2013, 2015; Robinson & Espaillat 2019; Pittman et al. 2022).

The accretion onto CTTSs is known to be intrinsically variable on timescales of minutes–hours (e.g., inhomogeneous accretion flows, hot-spot plasma oscillations), days–weeks (e.g., inner disk inhomogeneity, inner disk thermal instabilities), and months–years (e.g., MRI, gravitational instability); see review by Bae et al. (2022). Observationally, the variable mass accretion process is often associated with other sources of variability, including stellar rotation, chromospheric activity, disk occultation, variable extinction, winds/outflows, dark spots, and flares.

Accretion has been correlated with UV (Calvet et al. 2004; Ardila et al. 2013; Robinson & Espaillat 2019) and optical (Alcalá et al. 2014, 2017) line luminosity, though there is typically notable scatter/outliers within these empirical relationships, implying that they are an imperfect analog for the true accretion rate. One explanation for this scatter is intrinsic variability, though until now no extensive multiepoch far-UV (FUV)/near-UV (NUV) campaign has been carried out to gauge how these relationships vary in individual stars as the accretion varies over the span of several rotation periods.

In an effort to better understand accretion variability in CTTSs and to connect it to other observables in the UV–IR, a multiwavelength, multiepoch observing campaign of the CTTSs TW Hya, RU Lup, BP Tau, and GM Aur was carried out in 2021 and 2022. These observations include multiepoch HST Cosmic Origins Spectrograph (COS) UV spectra taken as part of the UV Legacy Library of Young Stars as Essential Standards (ULLYSES) HST Director's Discretionary Time Program; moderate-cadence, multiband *uBgVriz* and Transiting Exoplanet Survey Satellite (TESS; Ricker et al. 2015) photometry; and multiepoch, high-resolution optical spectra. In this paper (Paper I) we present the HST COS FUV and NUV results of our multiepoch, multiwavelength study of these four CTTSs. The photometry and optical spectra, partly obtained as part of the Outflows and Disks around Young Stars: Synergies for the Exploration of ULLYSES Spectra (ODYSSEUS) collaboration and the PENELLOPE Very Large Telescope (VLT) program (Manara et al. 2021; Espaillat et al. 2022), will be presented in follow-up works, Papers II and III, respectively.

Here in Paper I, we describe our sample in Section 2 and then our observations and data in Section 3. Section 4 describes our accretion shock model and the results of our analyses. In Section 5, we discuss these results in more detail and speculate on their implications. We summarize our final conclusions in Section 6.

2. Sample

Our sample consists of TW Hya, RU Lup, BP Tau, and GM Aur, chosen by the ULLYSES implementation team. This sample was chosen because they are well-studied, prototypical CTTSs with well-known magnetic configurations and reasonably constrained rotation periods. Below we provide more background information on each target, with some properties summarized in Table 1.

2.1. TW Hya

TW Hya is a nearby ($d \sim 60$ pc; Gaia Collaboration et al. 2023) CTTS of spectral type K7 (Ingleby et al. 2013). Its surrounding disk has many concentric gaps and rings (Andrews et al. 2012; Huang et al. 2018a), which may have been carved out by an embedded planet (Nayakshin et al. 2020; Zhu et al. 2023). The star is viewed nearly pole-on (18°, from $v\sin i$;

Alencar & Batalha 2002), and the disk is viewed nearly face-on (5°.5–7°, from scattered light and (sub)millimeter continuum; Qi et al. 2004; Huang et al. 2018a; Debes et al. 2023). We adopt an inclination of 7° from millimeter observations here and in Papers II and III. Donati et al. (2011) estimate the star's magnetic obliquity, the angle between its rotation and dipolar magnetic axis, to be low, at about 10°.

Despite its nearly pole-on geometry, TW Hya has shown photometric periodicity, though at a wide and inconsistent range of periods (0.16–4.7 days; Siwak et al. 2011, 2014, 2018). Radial velocity studies (Huélamo et al. 2008; Sicilia-Aguilar et al. 2023) reveal a strong, stable, sinusoidal rotational modulation at about 3.57 days.

TW Hya is old (8–10 Myr; Sokal et al. 2018), yet it is still actively accreting from a surrounding accretion disk beyond the assumed $\lesssim 5$ Myr life span of protoplanetary disks (Evans et al. 2009; Williams & Cieza 2011) and therefore challenges our understanding of disk dispersal mechanisms. The range of measured accretion rates in TW Hya is (0.05–0.6) $\times 10^{-8}$ $M_\odot$ yr^{-1} (Ingleby et al. 2013; Manara et al. 2014; Robinson & Espaillat 2019; Herczeg et al. 2023; Sousa et al. 2023). This accretion is thought to primarily occur through a single, large, poleward flow (Donati et al. 2011; Sicilia-Aguilar et al. 2023), along with many smaller, more sporadic accretion tongues near the equator (Siwak et al. 2018).

2.2. RU Lup

Previous studies of RU Lup have shown that it is a highly veiled ($r_K = 6.3$, $r_V = 2$–9; Stempels & Piskunov 2002; Stempels et al. 2007; Herczeg & Hillenbrand 2008; Sousa et al. 2023), strongly accreting ($\dot{M} \sim (2$–$7) \times 10^{-8}$ $M_\odot$ yr^{-1}; Herczeg et al. 2005; Herczeg & Hillenbrand 2008; Alcalá et al. 2017; Stock et al. 2022) K7 (Sousa et al. 2023) CTTS with a powerful accretion-driven outflow (Takami et al. 2001; Whelan et al. 2021). Its distance is about 156 pc (Gaia Collaboration et al. 2023). The rotation period of RU Lup is generally assumed to be 3.71 days (Stempels et al. 2007), detected via radial velocity measurements. However, this period has not been recovered in other time-dependent photometric studies of RU Lup, likely due to the combination of stochastic accretion activity (Siwak et al. 2016; Stock et al. 2022) and its low inclination angle.

RU Lup possesses a 63 au radius dust disk (with a gas disk extending to 120 au) with concentric gaps and rings (Andrews et al. 2018; Huang et al. 2018b) and unique gas structure. The gas structure, primarily traced by ^{12}CO, is a large, clumpy five-armed spiral that extends for >1000 au (Huang et al. 2020b). Millimeter continuum (Huang et al. 2018b) and near-IR (NIR; *K*-band) interferometric (GRAVITY Collaboration et al. 2021) observations find disk inclinations of 18°.8 and 16°, respectively. Other observations of RU Lup have placed the stellar inclination between 23° and 24° using line broadening (Herczeg et al. 2005) and radial velocity variations (Stempels et al. 2007), slightly higher than the millimeter observations, but still in line with a close-to-face-on disk. Here we assume an inclination of 16° from millimeter observations.

2.3. BP Tau

BP Tau is a ~3 Myr (Grankin 2016) K7 (Ingleby et al. 2013) system in the Taurus-Auriga complex at a distance of about 128 pc (Gaia Collaboration et al. 2023). Previous studies have estimated a wide range of accretion rates for BP Tau, in the range of (0.09–3) $\times 10^{-8}$ $M_\odot$ yr^{-1} (Gullbring et al. 1998; Schmitt et al. 2005; Long et al. 2011; Ingleby et al. 2013). Its rotation period has been estimated to be between 6.1 and 11 days (Vrba et al. 1986; Simon et al. 1990; Osterloh et al. 1996; Gómez de Castro & Franqueira 1997; Percy & Palaniappan 2006; Percy et al. 2006), but it is generally considered to be either 7.6 or 8.2 days from photometric variability, assumed to originate from accretion signatures rotating with the stellar surface.

Donati et al. (2008) performed a spectropolarimetric study of BP Tau in 2006 to map the structure of its magnetic field. Their study revealed a field dominated by a dipolar component, but still with a strong octupolar component, both tilted from the rotation axis by ~10°, though in opposite directions. They predicted accretion hot spots on its surface near the octupoles that cover about 2% of the surface. Long et al. (2011) also recovered similar accretion structure, revealing that the hot spots are mostly symmetric in longitude but elongated in latitude.

Observations of BP Tau's disk reveal a ~60 au radius dust disk with two to three gap/ring pairs inclined at 37°–39° (Long et al. 2019; Zhang et al. 2023). The stellar inclination has also been estimated at 48°–52° (Simon et al. 1990; Johns-Krull et al. 1999) from estimates of $v\sin i$ and an assumed rotation period of 7.6 days. We adopt an inclination of 38°.2 from the millimeter observations of Zhang et al. (2023).

2.4. GM Aur

GM Aur is a young (2 Myr; Jensen & Mathieu 1997) K5 (Manara et al. 2014) system in the Taurus-Auriga complex at a distance of about 155 pc (Gaia Collaboration et al. 2023). It possesses a transitional disk with an inner cavity of radius 20 au and multiple outer concentric rings (Espaillat et al. 2011; Macías et al. 2018; Huang et al. 2020a). Such studies place the disk inclination between 52°.8 and 53°.2, and we adopt 53°.

It is a moderate accretor, with accretion rates in the range (0.4–2.0) $\times 10^{-8}$ $M_\odot$ yr^{-1} (Ingleby et al. 2013; Manara et al. 2014; Robinson & Espaillat 2019; Espaillat et al. 2021). The accretion occurs primarily via a single, large hot spot near the pole that, in combination with its moderate inclination and rotation, causes a strong, stable periodicity of about 6 days (Percy et al. 2010; Espaillat et al. 2021; Bouvier et al. 2023). The magnetic obliquity has been estimated at 13° (McGinnis et al. 2020).

Espaillat et al. (2021) showed that short-wavelength photometry (*ug*) peaked about a day prior to longer-wavelength bands (*ri*/TESS), which they attribute to a large, asymmetric, and azimuthally stratified accretion hot spot. Bouvier et al. (2023) recently conducted a multiwavelength study of GM Aur in 2021, including optical/NIR photometry and spectra. They found a ~6 days period in their photometry, as well as at low redshifted velocities (~0–100 km s^{-1}) in Hα, Hβ, and Hγ and in the wings (±200–400 km s^{-1}) of Hα and Hβ. At moderate blueshifted velocities (−200 to 0 km s^{-1}), where variable absorption is strongest, they found nonperiodic variability. They attribute these variability characteristics (both periodic and nonperiodic) to the presence of a stable, rotating accretion hot spot along with stochastically variable outflows.

3. Observations and Data Reduction

HST observations were carried out with the COS instrument for TW Hya, RU Lup, BP Tau, and GM Aur as part of the

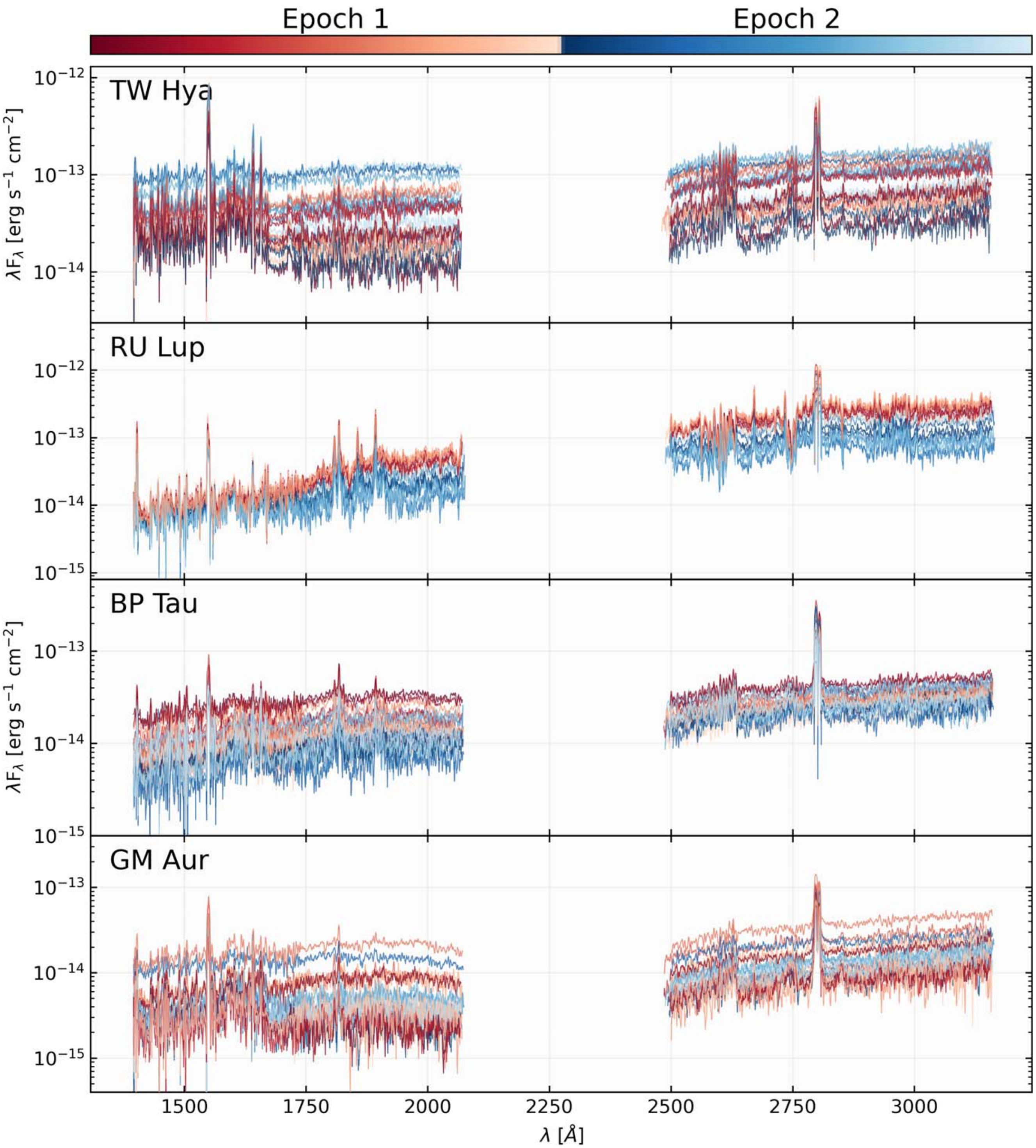

Figure 1. HST COS spectra of TW Hya, RU Lup, BP Tau, and GM Aur. The red spectra were taken in Epoch 1, while the blue spectra were taken in Epoch 2. Darker lines denote spectra obtained earlier in their respective epoch. Spectra have not been dereddened here. For clarity, data have been smoothed using a Savitzky–Golay filter. More details on the timing of the observations are given in Table 2.

ULLYSES DDT program through proposals 16107–16110 and 16589–16592 (Roman-Duval et al. 2020; PI: Julia Roman-Duval). These spectra are presented in Figure 1. The observations utilized the G160M and G230L gratings, which cover a wavelength range of about 1400–3200 Å, with a gap between about 2100 and 2500 Å. Below about 1760 Å the spectral resolution, R, is ∼18,000, and elsewhere $R \sim 2900$. All spectra have been dereddened according to the Whittet et al. (2004) extinction law and the extinction values from Table 1, assuming $R_V = 3.1$. The spectra presented here were obtained via ULYSSES Data Release 6 (Roman-Duval et al. 2020). Note that a portion of the TW Hya data used here is presented in Hinton et al. (2022) in a study of flaring in CTTSs.

Each target was observed approximately four times per rotation period for three rotation periods in two epochs separated by about a year (see Table 2), totaling 21–24 visits

Table 2
HST COS Observations

Object	Epoch	Date (UT) (Begin/End)	MJD (Begin–End)	No. of Observations
TW Hya	1	2021-03-29/2021-04-08	59302.7–59312.6	11
TW Hya	2	2022-03-30/2022-04-27	59668.5–59695.4	10
RU Lup	1	2021-08-10/2021-08-21	59436.9–59447.3	10
RU Lup	2	2022-08-10/2022-08-24	59801.3–59815.4	12
BP Tau	1	2021-08-20/2021-09-12	59446.8–59469.1	12
BP Tau	2	2022-12-13/2023-01-06	59926.2–59950.5	12
GM Aur	1	2021-10-13/2021-12-12	59500.5–59560.2	11
GM Aur	2	2022-11-26/2022-12-12	59909.9–59925.2	11

Note. All HST spectra used in this work, including targets and templates, can be found in MAST doi:10.17909/a530-qm96.

per target. All HST spectra used in this work can be found in MAST doi:10.17909/a530-qm96. For clarity, in this work "epoch" will refer to the different halves of the monitoring (Epoch 1/E1 corresponding to 2021 and Epoch 2/E2 corresponding to 2022/2023), while "visit" will refer to individual HST observations.

There were some changes to the observing schedule of the targets, typically due to problems with guide star and/or target acquisition. Several visits of TW Hya failed during the original scheduled window in E2 and were rescheduled to 2022 April 25–26 (MJD: 59694.5–59695.4). HST went offline during a visit of GM Aur on 2021 October 5 (MJD: 59492) in E1. The remaining observations were carried out during 2021 December 6–12 (MJD: 59554.3–59560.2). In other cases, individual observations failed and were not reobserved, resulting in fewer than 24 total observations for each target, except BP Tau, for which all 24 total observations were carried out.

4. Analysis and Results

In the following subsections we analyze and model the UV spectra presented in Section 3. We characterize the accretion properties of TW Hya, RU Lup, BP Tau, and GM Aur by fitting the data with accretion shock models. We measure the luminosities of UV lines and features and compare these to the accretion rates derived with the accretion shock models.

4.1. Accretion Shock Modeling

We use the accretion shock models of Calvet & Gullbring (1998) following similar methods to those of Robinson & Espaillat (2019, hereafter RE19). We adopt the stellar parameters listed in Table 1.

To accurately estimate the excess emission caused by accretion, one must have an estimate of the underlying photospheric+chromospheric emission ($F_{\rm Phot,True}$) of a non-accreting star (see Equation (1), where $F_{\rm WTTS}$ is the raw spectrum of a nonaccreting weak T Tauri star (WTTS), $V_{\rm CTTS}$ and $V_{\rm WTTS}$ are the fluxes of the CTTS and WTTS spectra at V band (5500 Å), f_i is the surface coverage fraction of an individual accretion column i, and r_V is the optical veiling). To estimate this, we utilize contemporaneous optical veiling measurements (r_V) to scale a raw WTTS spectrum ($F_{\rm WTTS}$) to the appropriate V-band level for any visit with contemporaneous V photometry (see Paper II). We calculate veiling using medium-to-high-resolution ($R \sim 5400$–140,000) optical ($\lambda \sim$ 4000–8000 Å) spectra from SMARTS/CHIRON, VLT/ESPRESSO, VLT/XSHOOTER, VLT/UVES, Haute-Provence/SOPHIE, and Tautenberg/TCES. We follow the basic procedure of Hartigan et al. (1989). See Section 3 of Paper III for a more detailed description of our procedure and findings. For TW Hya, RU Lup, and BP Tau, we use HST STIS spectra of the K7 WTTS HBC 427 (PID 11616) as the basis for the photospheric template, while for GM Aur we use the K5 WTTS RECX-1 (PID 11616).

The result is the emission from the fraction of the stellar photosphere not covered by accretion shocks ($F_{\rm Phot,Obs.}$) that contributes to the observed CTTS spectrum for that particular visit. We can then fit for the excess emission due to accretion (see below) and divide $F_{\rm Phot,Obs.}$ by the fraction of the stellar surface not covered by hot spots to obtain $F_{\rm Phot,True}$, which can be used for fitting. This results in multiple photospheric templates for each target (with the exception of RU Lup), one for each visit with contemporaneous V-band observation. We obtain 21 templates for TW Hya, 15 for BP Tau, and 14 for GM Aur.

$$F_{\rm Phot,True} = F_{\rm WTTS}\left(\frac{V_{\rm CTTS}}{V_{\rm WTTS}}\right)\left(\frac{1}{1+r_V}\right)\left(\frac{1}{1-\sum f_i}\right). \quad (1)$$

In the case of RU Lup, we are unable to estimate r_V for any visit, due to the numerous strong emission lines in its optical spectra (see Paper III; Gahm et al. 2008). We therefore cannot estimate $F_{\rm Phot,True}$ as above. Instead, we assume that $F_{\rm Phot,True}$ is the raw HST spectrum of HBC 427 ($F_{\rm WTTS}$) scaled to the distance and radius of RU Lup via Equation (2). We discuss this further in Appendix A.

$$F_{\rm Phot,True} = F_{\rm WTTS}\left(\frac{d_{\rm WTTS}R_{\rm CTTS}}{d_{\rm CTTS}R_{\rm WTTS}}\right)^2. \quad (2)$$

To reproduce the excess emission, here we follow Ingleby et al. (2013) and use multiple accretion columns. We employ a four-column model with energy fluxes, $\mathcal{F} = 1/2\rho v_s^3$, of 10^{10} (low), 10^{11} (medium), 10^{12} (high), and 3×10^{12} (very high) erg s^{-1} cm^{-2}. RE19 note that the inclusion of this fourth, very high density column was necessary for several observations of DM Tau and GM Aur to fit the spectrum near 1800 Å. Here we use four columns for all of our fitting for consistency. The energy flux ($\mathcal{F}$) depends on ρ, the density of material in the accretion column, and v_s, the infall velocity. The infall velocity is set to be the freefall velocity at the magnetospheric truncation radius ($R_{\rm in}$) of 5 stellar radii. We note that $R_{\rm in}$ has been measured in

TW Hya ($3.5R_\star$, Gravity Collaboration et al. 2020; $8.3R_\star$–$12.4R_\star$ depending on assumed magnetic field strength, Gravity Collaboration et al. 2023) and RU Lup ($3.3R_\star$–$6.6R_\star$ depending on assumed magnetic field strength; Gravity Collaboration et al. 2023). We opt to use $5R_\star$ for all objects, due to the uncertainties in these estimates and for consistency; the freefall velocity changes little for any choice of $R_{\rm in}$ within the measured uncertainties.

We use filling factors (f_i) to scale the resulting emission, and these are left as free parameters. These four filling factors ($f_{\rm low}$, $f_{\rm medium}$, $f_{\rm high}$, $f_{\rm very\ high}$) measure the fraction of the visible stellar surface that is covered by the four accretion columns with the energy fluxes noted above. We calculate $\dot{M}$ by adding the contributions of the four accretion columns with

$$\dot{M} = \frac{8\pi R_*^2}{v_s^2}\sum_i \mathcal{F}_i f_i = \frac{8\pi R_*^2}{v_s^2}\mathcal{F}_{\rm weighted} f_{\rm total}. \quad (3)$$

One can additionally calculate the fractional accretion rate ($\dot{m}_k$) for each column as the fraction of the total mass accretion rate contributed by that individual column,

$$\dot{m}_k = \frac{f_k \mathcal{F}_k}{\sum_i f_i \mathcal{F}_i}, \quad (4)$$

where f is the filling factor and $\mathcal{F}$ is the associated energy flux.

We resample our COS spectra to a lower resolution ($R \sim 1500$, similar to that of the HST STIS G230L grating used in Robinson & Espaillat 2019) and mask notable lines (e.g., Mg II: 2800 Å). We also remove data below ∼1800 Å, due to the abundance of emission lines and added uncertainty in estimating the continuum. Including some optical emission is important to constrain the contribution from lower-density columns, which can cover a large fraction of the star and contribute significantly to the total mass accretion. While RE19 use HST STIS NUV–optical spectra, which extend continuously from ∼1800 to 5700 Å, our HST COS spectra extend to just 3200 Å and so do not span any optical wavelengths. Thus, we combine our COS spectra with contemporaneous (within 6 hr) *BgV* photometry (see Paper II). We do not include anything redder than *V* (such as *ri*) since we truncate our model at 5700 Å. Visits without contemporaneous photometry are still modeled in the same manner and are noted in Tables 4 and 5, but they should be considered carefully, and we discuss the reliability of these results in Appendix B.

Based on modeling that has shown that accretion hot spots can cover up to ∼40% of the stellar surface (Romanova et al. 2003; Ingleby et al. 2013, 2015; Robinson & Espaillat 2019), we allow individual f_i to vary between 0% and 40% and limit the total surface coverage of all columns (Σf_i) to 50%. The accretion column filling factors are fit using a Markov Chain Monte Carlo (*emcee*; Foreman-Mackey et al. 2013) technique.

Every HST visit for a given target is fit with each template for that target. For example, each of the 24 visits of BP Tau was fit using each of the 15 templates. The final value for a given parameter in a single fit is the median of the posterior distribution, and the upper/lower uncertainties are the difference between the 84th/16th percentile and the median ($\pm 1\sigma$). Finally, these values and uncertainties are averaged across all templates, resulting in the values listed in Tables 4 and 5.

Figure 2 shows the results of our shock modeling, including accretion rates, filling factors (f), and fractional accretion rates ($\dot{m}$) of the four accretion columns. Individual fits for each HST visit can be found in Figures 7–14 in Appendix C. In most cases there are anticorrelations in the posterior distributions of adjacent accretion columns ($f_{\rm Low}/f_{\rm Medium}$, $f_{\rm Medium}/f_{\rm High}$, and $f_{\rm High}/f_{\rm Very\ \ High}$) resulting from degeneracies between the models. Some degeneracy is expected, given that the emission from like-density accretion columns is similar. We discuss the details of the fits for each individual object in the subsections below.

4.1.1. Modeling Results for TW Hya

TW Hya's accretion is primarily driven by the low-density accretion column, which generally covers 20%–40% of the stellar surface and contributes 40%–70% of the total mass accretion. In some cases, the medium-density column becomes significant (often when $f_{\rm Low}$ is very low, likely due to their degeneracy) and can contribute up to 90% of the mass accretion, though it typically covers ∼1% of the surface and contributes 0%–50% of the mass accretion. The high-density column consistently contributes 10%–50% of the mass accretion, while the very high density column is generally insignificant in TW Hya, except for two visits of high $\dot{M}$ in E2.

While the total mass accretion is typically dominated by the lower-density columns, the variability in the accretion appears to be driven by the high-density columns. The Spearman r coefficient between $\dot{m}_{\rm Low+Medium}$ and $\dot{M}$ is −0.74, while it is +0.74 between $\dot{m}_{\rm High+Very\ High}$ and $\dot{M}$, suggesting that changes in the accretion are driven by higher-density, hotter accretion flows. For reference, $r = 1$ implies a perfect positive correlation, $r = -1$ implies a perfectly negative correlation, and $r = 0$ implies no correlation.

Overall, the accretion rate (top left panel, uppermost row, Figure 2) varies in the range $(0.08–0.51) \times 10^{-8}\ M_\odot\ {\rm yr}^{-1}$ peak to peak across both epochs, a factor of 6.5 difference (0.80 dex), with a median accretion rate of $0.25 \times 10^{-8}\ M_\odot\ {\rm yr}^{-1}$. The median accretion parameters and variability are similar in E1 and E2, with TW Hya accreting more strongly in E2 ($0.23 \times 10^{-8}\ M_\odot\ {\rm yr}^{-1}$ vs. $0.35 \times 10^{-8}\ M_\odot\ {\rm yr}^{-1}$).

4.1.2. Modeling Results for RU Lup

RU Lup (top right panel of Figure 2) is the strongest accretor in our sample, with accretion rates in the range $(11.8–17.0) \times 10^{-8}\ M_\odot\ {\rm yr}^{-1}$ in E1, with a median of $13.2 \times 10^{-8}\ M_\odot\ {\rm yr}^{-1}$. The accretion rate drops considerably from E1 to E2, with rates in the range $(3.5–12.2) \times 10^{-8}\ M_\odot\ {\rm yr}^{-1}$ in E2 and a median of $6.0 \times 10^{-8}\ M_\odot\ {\rm yr}^{-1}$. The peak-to-peak variability in RU Lup is a factor of 4.9, or 0.69 dex.

The accretion is dominated by the medium-density column in both E1 and E2. In E1, it covers 18%–26% of the stellar surface and contributes 85%–98% of the total mass accretion rate. In E2, it covers 6.9%–19.4% of the surface and contributes 80%–97% to $\dot{M}$. The decrease in $\dot{M}$ from E1 to E2 is driven entirely by the decrease in $f_{\rm Medium}$. No other accretion column contributes more than 16% of the accretion in any visit. Combined, $\dot{m}_{\rm Low}$, $\dot{m}_{\rm High}$, and $\dot{m}_{\rm Very\ High}$ contribute just 4.6% of the mass accretion on average.

4.1.3. Modeling Results for BP Tau

BP Tau is a moderate accretor, with accretion rates in the range $(0.9–3.2) \times 10^{-8}\ M_\odot\ {\rm yr}^{-1}$ in E1 and $(0.9–1.7) \times 10^{-8}\ M_\odot\ {\rm yr}^{-1}$ in E2 and median accretion rates of 1.3 ×

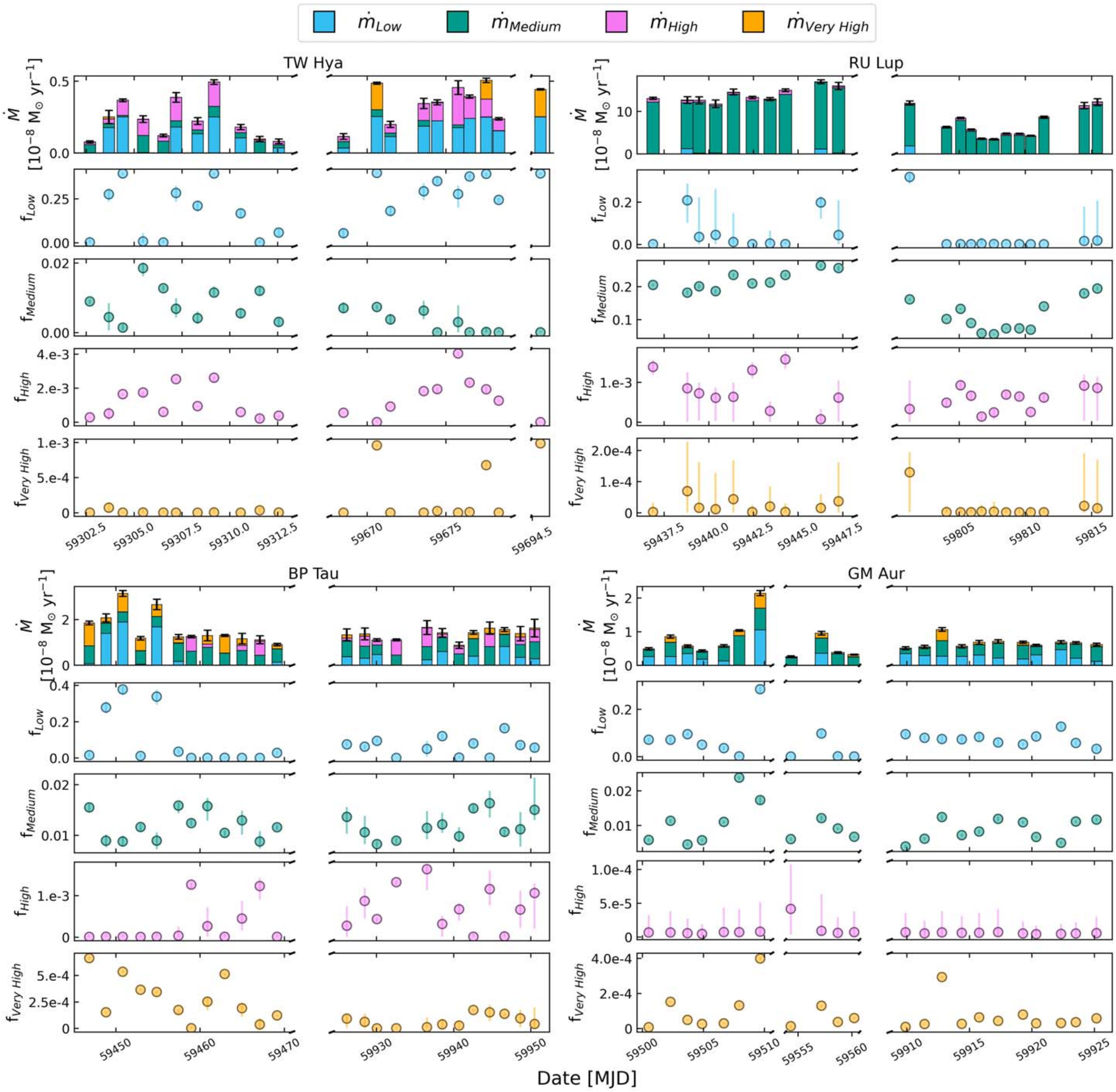

Figure 2. Results of our shock model fitting for TW Hya (top left), RU Lup (top right), BP Tau (bottom left), and GM Aur (bottom right). The upper row of each panel shows the mass accretion rate; the total height of the bar represents the total accretion rate, while the colored bars show the accretion contributed by each respective accretion column. The error bar atop each bar represents the uncertainty on the total accretion rate. The subsequent rows are the filling factors of the low, medium, high, and very high density accretion columns. The left and right columns of each panel show Epochs 1 and 2, respectively. Note the additional break in the Date axes for TW Hya E2 and GM Aur E1 due to the uneven sampling from HST.

$10^{-8}\ M_\odot\ \mathrm{yr}^{-1}$ and $1.4 \times 10^{-8}\ M_\odot\ \mathrm{yr}^{-1}$, respectively. Overall, the accretion rate varies by a factor of 3.6 (0.55 dex) peak to peak.

The medium-density column typically dominates the accretion in BP Tau, covering 1%–2% of the stellar surface and accounting for 40%–60% of the mass accretion. That said, each column, in at least one visit each, contributes >50% to $\dot{M}$ in that visit, suggesting that all columns are important. This is reinforced by the fact that the r correlation coefficient does not exceed 0.4 for the lower/higher-density columns in either E1 or E2, showing that no one column consistently dominates the total accretion rate.

From E1 to E2, the accretion appears to become cooler/less dense. The low- and high-density columns, on average, contribute more to the accretion, while the very high density column diminishes. This can be qualitatively observed in Figures 11 and 12 in Appendix C, where the slope of the BP Tau spectra in E1 appears flatter than that in E2, implying a hotter/denser accretion flow in E1.

4.1.4. Modeling Results for GM Aur

GM Aur is dominated by low- and medium-density accretion columns that, save for the accretion burst near MJD = 59509 (discussed in more detail below), together fill up to 15% of the stellar surface and typically constitute 90% of the total mass accretion. The high-density accretion is largely insignificant, generally contributing <1% to the total accretion, with visit 1.7 being the only exception, where it jumps to 6.0%. While the very high density accretion column only contributes ∼10% to $\dot{M}$ on average, it is highly correlated with $\dot{M}$, with r values of 0.56 and 0.93 in E1 and E2, respectively. This is similar to TW Hya, where the bulk of the accretion comes from lower-density flows, but the variability is primarily driven by higher-density, hotter flows.

The accretion varies in the range (0.32–2.15) × 10^{-8} $M_{\odot}$ yr^{-1} in E1 (which includes a burst) and (0.5–1.1) × 10^{-8} $M_{\odot}$ yr^{-1} in E2. The median accretion rates are 0.58 × 10^{-8} $M_{\odot}$ yr^{-1} and 0.67 × 10^{-8} $M_{\odot}$ yr^{-1}, respectively. Most of the variability is driven by small bursts, with up to four seen in our HST observations at MJD ∼ 59502, 59509, 59557, and 59912. With the exception of the burst at MJD = 59509, they persist across only one HST visit (no more than 2 days) and increase $\dot{M}$ by about 0.5 × 10^{-8} $M_{\odot}$ yr^{-1}, or a factor of 2.

HST captured the beginning of the larger burst at MJD = 59509 in at least two visits, but due to synchronization problems with the command flow, it went into safe mode soon after and was unable to capture the end of the burst. The accretion rate increased from a quiescent rate of ∼0.43 × 10^{-8} $M_{\odot}$ yr^{-1} to 2.15 × 10^{-8} $M_{\odot}$ yr^{-1} within 4 days, a factor of 5.0 (0.70 dex) increase. This burst (and the smaller ones discussed above) was driven by the very high density accretion column, for which $\dot{m}_{\mathrm{Very\ High}}$ increased by about a factor of 3.5 over that time.

4.2. UV Spectral Lines and Features

UV line luminosities have previously been found to correlate with mass accretion (Calvet et al. 2004; Yang et al. 2012; Ardila et al. 2013; Ingleby et al. 2013; Robinson & Espaillat 2019). Additionally, a broad region near 1600 Å dubbed the "H_2 bump" (e.g., Bergin et al. 2004; Herczeg et al. 2004) has also been linked to accretion (see Ingleby et al. 2009, 2012; Yang et al. 2012; France et al. 2017, 2023; Thanathibodee et al. 2018; Espaillat et al. 2019). Here we measure the luminosities of selected UV lines, the FUV and NUV continua, and the H_2 bump.

4.2.1. UV Line Luminosities

While these COS spectra are filled with many emission lines, we focus on 11 of the brightest lines previously linked with accretion (see Table 3). Note that many of these lines are blended and only approximate line centers are provided in Table 3. Additionally, Mg II is affected by wind absorption (Ardila et al. 2002; Xu et al. 2021). To measure the line luminosities, we first subtract the continuum from the dereddened spectra. Within ∼50 Å of the line center, we mask outlying points above or below the median flux of the spectrum, where the outlier threshold varies per line and per object. We then fit a continuum to the remaining data using the *specutils* function *fit_generic_continuum* and subtract this from the original spectrum. We then integrate the flux of the continuum-subtracted spectrum within a narrow region that varies by line. Finally, we convert these fluxes to luminosities.

Table 3
UV Features

Line	λ_0 (Å)	Approx. Width (Å)
Mg II[a]	2798	20
Al III]	2670	10
C III]	1909	10
Si III]	1892	5
Si II	1808	10
O III]	1666	5
He II	1640	5
C IV[a,b]	1548	8
C I[b]	1463	2
Si IV[b]	1403	4
Si III[b]	1399	2
H_2 bump	1600	200

Notes.
[a] We do not separate the doublet components of the Mg II and C IV lines. Central wavelengths noted here are the short-wavelength component of the doublet.
[b] These lines are blended with H_2 lines (France et al. 2012).

Figure 3 shows our UV luminosities along with log–log linear relationships with L_{acc} (Equation (5)) derived here. We exclude nondetections (here defined as signal-to-noise ratio (SNR) < 2) in Figure 3 and in the associated linear fits. UV luminosities, fit coefficients, and associated uncertainties are shown in Tables 6–10.

$$L_{\mathrm{acc}} = \frac{GM_{*}\dot{M}}{R_{*}}\left(1 - \frac{1}{R_i}\right),\ R_i = 5R_{*}. \qquad (5)$$

Looking at all objects together, only three lines exhibit moderate correlations to L_{acc}, Mg II (r = 0.66), Al III] (r = 0.55), and Si III] (r = 0.61), though Si III] is often only marginally detected, despite this global correlation. The other lines show weak/no correlation and are often skewed by TW Hya and/or RU Lup. L_{acc} in TW Hya is comparable to BP Tau and GM Aur, but in many cases it exhibits much brighter emission lines. L_{acc} is much higher in RU Lup, but its lines are often significantly dimmer than would be expected given its accretion rate (particularly He II, C IV), rendering those global correlations very weak.

If, instead, we focus on the interobject trends, many object −line pairs show strong correlations that differ from the global trend or exist when a global trend does not. TW Hya shows weak to moderate correlations in all lines except He II (r = 0.85) and C IV (r = 0.86), which are strongly correlated to L_{acc}. In RU Lup, some lines (Al III], Si III], Si IV) show strong correlations to L_{acc}, but others show no or even anticorrelation. He II is actually moderately anticorrelated with L_{acc} (r = −0.49) and is exceptionally dim relative to other lines and targets. BP Tau in all cases shows weak correlations between L_{acc} and L_{Line}, though Mg II is moderately correlated (r = 0.59). The UV lines in GM Aur do not show any particularly strong correlations with L_{acc}, with Mg II, He II, and C IV showing the strongest correlations at r = 0.75, 0.67, and 0.81, respectively. The others are weakly correlated or have large uncertainties, due to so many visits being discarded as nondetections (e.g., Al III], C III, Si III], O III]).

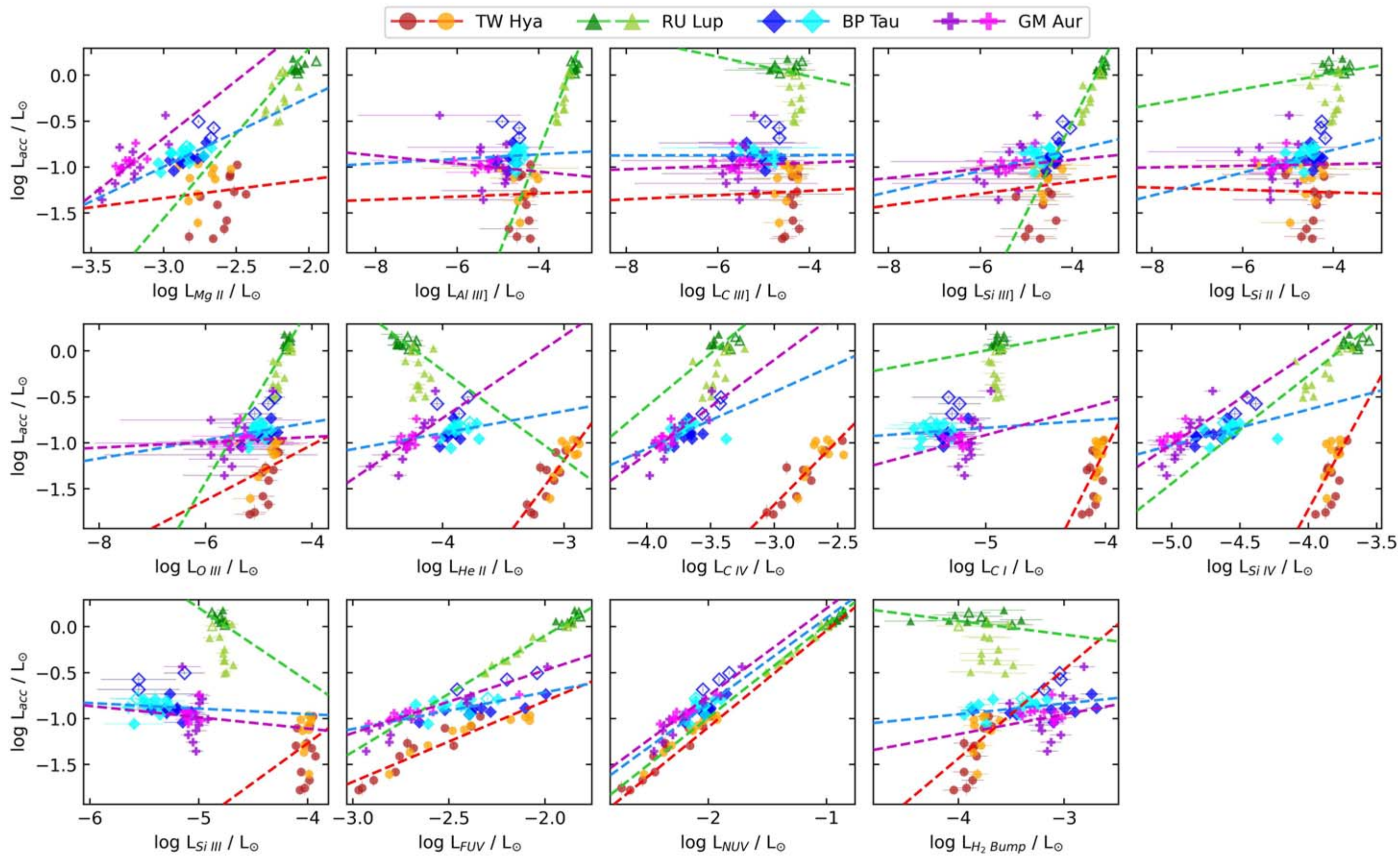

Figure 3. Accretion luminosity vs. luminosity for various UV lines/regions. Red/orange circles, green/lime triangles, blue/cyan diamonds, and purple/pink plus signs represent TW Hya, RU Lup, BP Tau, and GM Aur, respectively. Open points are visits without contemporaneous photometry. Colored, dashed lines are the intra-object log–log linear fits for all observations of each target (see Table 10). For all UV features besides the H_2 bump, we exclude data with SNR < 2. For the H_2 bump, we only exclude data where the bump was not visually detected, independent of SNR.

4.2.2. FUV and NUV Continuum Luminosities

For the FUV and NUV fluxes, we integrate the flux of the fitted, dereddened continuum spectra in the ranges 1400–2100 Å and 2500–3200 Å, respectively. The FUV and NUV luminosities and fit coefficients are listed in Tables 6–9 in the appendice and in Figure 3.

TW Hya shows a wide range of FUV luminosities, ranging between $0.005L_\star$ and $0.040L_\star$ in both epochs, with a median of $0.014L_\star$ ($0.003\ L_\odot$). The NUV varies between $0.009L_\star$ and $0.056L_\star$, with a median of $0.028L_\star$ ($0.006\ L_\odot$). RU Lup is generally brighter than TW Hya and varies between $0.008L_\star$ and $0.026L_\star$ (median $0.020L_\star$, $0.015\ L_\odot$) in the FUV and between $0.052L_\star$ and $0.238L_\star$ (median $0.169L_\star$, $0.124\ L_\odot$) in the NUV. BP Tau shows the least degree of continuum variability, varying between $0.002L_\star$ and $0.011L_\star$ (median $0.004L_\star$, $0.003\ L_\odot$) in the FUV and between $0.007L_\star$ and $0.016L_\star$ (median $0.010L_\star$, $0.008\ L_\odot$) in the NUV. $L_{\rm FUV}/L_{\rm NUV}$ is on average higher in E1 (0.52) than in E2 (0.39), reinforcing the denser flow in E1 predicted by the shock model. GM Aur is generally the dimmest among the four targets, ranging between $0.0009L_\star$ and $0.008L_\star$ (median $0.0014L_\star$, $0.002\ L_\odot$) in the FUV and between $0.003L_\star$ and $0.010\ L_\star$ (median $0.005L_\star$, $0.006\ L_\odot$) in the NUV.

The FUV/NUV luminosities also show stronger time variability than the accretion rates, readily varying by a factor of 2 on day-long timescales. TW Hya exhibits a factor of ∼5.1 increase in FUV flux within just 2 days, from $7.3 \times 10^{-3}L_\star$ in visit 2.1 to $37.2 \times 10^{-3}L_\star$ in visit 2.2. The FUV and NUV continua rise considerably in GM Aur during the burst near MJD = 59509, by a factor of 8.5 and 4.7, respectively, in about 4 days.

The FUV/NUV continuum luminosities show far stronger correlations with $L_{\rm acc}$ than any of the lines, though some of the same trends persist. Globally, both $L_{\rm FUV}$ and $L_{\rm NUV}$ are strongly correlated with $L_{\rm acc}$, with $r = 0.85$ and 0.96, respectively. In the FUV, RU Lup again skews the fit, having either elevated accretion rates or diminished FUV luminosities. In the NUV all four targets exhibit similar slopes, though the y-intercept of the fitted line varies by target. Individually, each target (with the exception of BP Tau) shows fairly strong correlations with $L_{\rm acc}$: $r \geqslant 0.88$ in all cases. BP Tau is moderately correlated ($r_{\rm FUV/NUV} = 0.55/0.66$) but shows the same linear slope as the other targets in the NUV.

4.2.3. H_2 Bump Luminosities

For the H_2 bump near 1600 Å, we follow a similar method to that of France et al. (2017) to extract the bump spectrum and calculate its luminosity. We first hand-pick ∼110 points between 1400 and 1800 Å selected to avoid strong atomic and molecular lines. The lines present in each target vary, and so we change the selected points for each target. From these ∼110 points, we define a binned spectrum whose flux and uncertainty are the mean and standard deviation of the original spectrum within 0.75 Å of the selected points. This binned spectrum is thus a pseudocontinuum, composed of the true, underlying continuum plus the broad H_2 bump feature, and so does not include bright emission lines.

From this binned spectrum, we fit a continuum using a second-order polynomial using the points away from the H_2 bump, in the ranges 1405–1490 Å and 1690–1800 Å. Next, we subtract this continuum from the binned spectrum. Finally, we integrate this continuum-subtracted binned spectrum between 1490 and 1690 Å to calculate the H_2 bump flux and convert to luminosity. The H_2 bump luminosities are shown in Tables 6–9 and Figure 3 along with fit coefficients given in the appendices. For these correlations, we exclude data where the bump was not visually distinct from the underlying continuum, regardless of the calculated flux or SNR.

Note that while the measured uncertainties on the H_2 bump luminosities are low (typically <5%), the true uncertainties are likely higher. The determination of the continuum in each spectrum not only depends heavily on the number and location of the chosen binned continuum points but also can be affected by any spurious emission lines. For this reason, we apply an additional 10% uncertainty added in quadrature to the measured uncertainty for TW Hya, BP Tau, and GM Aur. RU Lup exhibits uniquely strong, wide, and numerous emission/absorption features, making its continuum particularly uncertain, so we apply a 20% uncertainty.

The H_2 bump shows similar trends to the other lines. TW Hya is the only target that shows a moderately positive correlation ($r = 0.54$). Here it is not an outlier and shows very similar bump luminosities to those of BP Tau and GM Aur. RU Lup shows a very weakly negative correlation and possesses much lower bump luminosities than the other targets with comparatively high $L_{\rm acc}$, though in most cases the bump is not detected. Even ignoring visit 1.7, with a particularly low bump luminosity, there is still only a weakly positive correlation in RU Lup. BP Tau shows a wide range of bump luminosities (∼1 dex) with no correlation to $L_{\rm acc}$, similar to many of the emission lines. The H_2 bump in GM Aur shows a very weakly positive correlation with $L_{\rm acc}$, with far more spread in $L_{\rm acc}$ than $L_{\rm H2\ bump}$. Globally, we see a weakly negative correlation between $L_{\rm acc}$ and $L_{\rm H2\ bump}$.

5. Discussion

Our shock model fitting finds diversity in accretion column structures between objects, but these structures remain roughly consistent for individual objects over the course of at least a year (i.e., the longest timescale probed in this work), while the accretion rate changes on short timescales of about a day. In TW Hya the shock model predicts a large hot spot dominated by the low-density accretion column, while in RU Lup the accretion is dominated by the medium-density accretion column. GM Aur is primarily dominated by the low- and medium-density columns, while BP Tau is marginally dominated by the medium-density column but sees strong contributions from the other columns at various times. Besides the fraction of the star covered by each column, there are no significant changes in these structures during the course of the HST observations, even when the accretion rate itself changes. Despite this relative stability in the accretion structure, there is variability in the accretion rate up to a factor of four within 2 days. This is consistent with previous reports that accretion is variable on all timescales probed (Costigan et al. 2014; Hartmann et al. 2016; Zsidi et al. 2022; Herczeg et al. 2023). Specifically, Venuti et al. (2014) find that accretion variability is typically about 0.5 dex on timescales of days–weeks, and our results are consistent with this. Our accretion rates are also within the scatter seen in accretion rate in larger samples (e.g., Manara et al. 2021). We see an average total surface coverage of about 15%, in line with magnetospheric accretion models that suggest total filling factors of about 20% (Zhu et al. 2023b).

TW Hya and GM Aur have been studied by other researchers with data sets overlapping the timing of the HST observations presented here, allowing us to directly compare our results. Herczeg et al. (2023) find that in over 25 yr of TW Hya optical spectroscopic data, with some that overlap the times of our data set, the average accretion rate is $0.25 \times 10^{-8}\ M_\odot\ {\rm yr}^{-1}$, which flickers over timescales of hours but is roughly stable over 25 yr and varies in the range $(0.05-0.9) \times 10^{-8}\ M_\odot\ {\rm yr}^{-1}$. Our results are consistent, and we find that the average accretion rate of TW Hya is about $0.3 \times 10^{-8}\ M_\odot\ {\rm yr}^{-1}$ with a range of $\sim(0.1–0.5) \times 10^{-8}\ M_\odot\ {\rm yr}^{-1}$. GM Aur was observed by Bouvier et al. (2023), who performed an optical and NIR spectrophotometric monitoring campaign overlapping some of the HST observations, probing timescales of days to months over a period of 6 months and covering 30 rotation periods. Bouvier et al. (2023) find evidence of rotational modulation of accretion and a stable accretion funnel flow and accretion shock. Our results are consistent with this study.

Some UV lines, such as the C IV line, have been seen to correlate with accretion rate in larger samples (e.g., Calvet et al. 2004; Yang et al. 2012; Ardila et al. 2013; Ingleby et al. 2013; Robinson & Espaillat 2019), but here we caution against using these lines alone to characterize the accretion rate. Like RE19 and Calvet et al. (2004), we do generally find a moderate, positive correlation between accretion rate and UV line luminosities. That said, certain targets (i.e., TW Hya, RU Lup) often deviate from these patterns. For some lines, the relationship between $L_{\rm line}$ and $L_{\rm acc}$ in TW Hya is consistent with the other targets, but in others it is completely removed from the other targets and the relationship described in RE19 and is self-consistent between E1 and E2. In these cases, either the accretion rates are lower than would be expected, or the UV luminosity is higher than expected. As for RU Lup, in only some cases (Mg II, Al III], Si III], Si IV) does it trend with other targets and previous studies. Even then, RU Lup exhibits a much steeper relationship than BP Tau, GM Aur, or the empirical relationships of Calvet et al. (2004), Yang et al. (2012), or RE19. The bright He II line is interesting, as it shows moderate anticorrelation and is rather dim when considering that RU Lup is comparatively bright in most lines and in $L_{\rm acc}$. TW Hya and RU Lup are outliers, and this may be linked to their viewing geometries, which are both seen closer to face-on (Table 1). Ultimately, while moderate correlations between $L_{\rm acc}$ and $L_{\rm UV}$ are generally found, we emphasize not only that there is considerable scatter in these relationships but also that the variability trends in individual targets often differ from the global trend. They should not be used to estimate accretion rates, at least on their own.

In the majority of cases, the correlation between observed flux (line or continuum) and accretion rate is positive. As more energy is available from a larger accretion rate, more power is radiated in the continuum and the line. If the structure of the accretion shock does not change with accretion rate, one might expect that the observed flux and accretion rate are directly proportional. However, in RU Lup, some line fluxes are observed to be anticorrelated with the accretion rate. Detailed multidimensional modeling with radiative transfer is beyond the scope of this work, but here we speculate on how this fits into our knowledge of accretion shock emission. Decreasing fluxes with increasing accretion luminosity are clearly seen in He II and Si III and less clearly in the H_2 bump and C III]. Thus, the conditions present in the medium-density accretion column (temperature, density, physical size, etc.) may promote a high optical depth for these lines. When the accretion rate increases in RU Lup, so does the size of the medium-density column, which may in turn increase the optical depth in these moderate-temperature lines, resulting in the negative relationships we see. Other lines, formed at lower (C I, Mg II) and higher (C IV) temperatures than the Si III and He II lines, would form in physically distinct locations and different conditions and may not be subject to the same optical depth effects as Si III and He II.

We also compare our results on the H_2 bump to those in the literature. The H_2 bump has been suggested to be driven by collisional excitation of H_2 via X-ray photons (Bergin et al. 2004), Lyα dissociation of H_2O in the inner disk (France et al. 2017), which has been linked to the surface density of the inner disk (Espaillat et al. 2019), or due to the H I two-photon continuum (Bottorff et al. 2006). Espaillat et al. (2019) found that there was no correlation between $L_{\rm H2\ bump}$ and contemporaneous X-ray data, and France et al. (2017) show that the H_2 bump spectrum itself is inconsistent with electron-impact excitation, ruling out the first scenario. For the last two scenarios, there is an expected correlation between the H_2 bump luminosity and $L_{\rm acc}$, since accretion should produce Lyα photons (e.g., Alencar et al. 2012). France et al. (2023) find strong correlations between the H_2 bump and both Lyα and Wide-field Infrared Survey Explorer W3−W4 colors, which they suggest reinforces that the H_2 bump originates in the inner disk, where Lyα photons can reach and dissociate the H_2O content of the inner disk. Espaillat et al. (2019) suggest that the H_2 bump is driven by changes in the surface density in the inner disk that propagate through the accretion column and lead to a change in the accretion rate. They find a strong correlation ($r = 0.7$) in a sample of seven CTTSs (27 observations). Looking at all four targets in our sample together (89 observations), we do not recover a strong (or even positive) correlation ($r = -0.42$) between the H_2 bump and $L_{\rm acc}$. Individually, the only target that shows even moderate correlation is TW Hya ($r = 0.54$). The other three targets show very weak correlations ($r \leqslant 0.31$). Therefore, we do not find strong evidence supporting that the H_2 bump is due to Lyα dissociation of H_2O or surface density changes.

Lastly, the FUV luminosity can change by a factor of 2–5 on day timescales and correlates well with accretion rate. While BP Tau shows comparatively little variability, the other three targets exhibit strong FUV/NUV continuum variability, about a factor of 10 peak to peak. The median FUV luminosity in our sample is 2.0×10^{31} erg s^{-1}, which is what is usually used in FUV photoevaporation models (e.g., Gorti et al. 2009; Pascucci et al. 2023). FUV radiation has also been shown to affect disk chemistry near planet-forming radii (Bergin et al. 2004; Yang et al. 2012; Ádámkovics et al. 2016). The FUV variability seen here implies that accretion-driven FUV radiation fields can reach levels 10× those assumed in Bergin et al. (2004), showing that accretion variability can drive disk chemistry dynamics.

6. Summary

We studied a multiepoch HST UV spectral monitoring campaign of four CTTSs: TW Hya, RU Lup, BP Tau, and GM Aur. We use a magnetospheric accretion shock model to estimate the accretion rates and accretion column filling factors for roughly 24 observations of each target. From those same spectra we measure luminosities of various UV lines, the 1600 Å H_2 bump, and the FUV/NUV continuum. Our main findings are as follows:

1. Our accretion shock modeling reveals an array of accretion structures in our four targets. Accretion in TW Hya is primarily driven by the low-density column, but some visits see strong contribution from other columns. RU Lup is dominated by medium-density accretion columns, with little accretion coming from other columns. BP Tau sees roughly equal contribution from all four columns, with a preference for the low- and medium-density columns. GM Aur is dominated by the low- and medium-density columns, with some contribution from the very high density column when the accretion rate increases.
2. All four targets show accretion variability of at least a factor of 3 (0.48 dex) during our monitoring. TW Hya and GM Aur exhibit variability in their accretion rate of a factor of 3 or greater within 2 days. RU Lup, on the other hand, shows a sustained decrease of a factor of 2.2 between 2021 and 2022, showing that CTTSs can undergo a sustained decrease in accretion rate on timescales of over 1 yr. BP Tau exhibited the least accretion variability in our sample, varying by about a factor of 3.6 peak to peak across all observations.
3. UV line luminosities are generally only moderately correlated with accretion rate, but TW Hya, RU Lup, and BP Tau often show scatter both with respect to other targets in the sample and within a single object. In TW Hya, the UV line luminosities are higher than expected given its low accretion rate. RU Lup is very inconsistent, showing no, strongly positive, and weakly negative correlations with accretion. We suggest that this is due to its strong accretion-driven outflow and/or near-face-on inclination. BP Tau generally shows little correlation to UV line luminosities; the accretion rate tends to vary significantly less than the line luminosities.
4. FUV and NUV continuum luminosities show strong correlations to accretion rate. TW Hya is again an outlier, with low accretion rates and high UV luminosities. Together, RU Lup, BP Tau, and GM Aur trend closely with one another. In general, the FUV/NUV continua are even more variable than the overall accretion rate, with both varying by factors of 2–5 within 1–2 days in all four targets.
5. We find generally comparable FUV luminosities to those used in previous works to estimate the effect of FUV radiation on disk dynamics, but note that accretion-induced variability can exceed this by a factor of ∼10 in some cases.
6. With the exception of TW Hya, we do not find strong correlations between accretion luminosity and the 1600 Å H_2 bump.

Our study further demonstrates that accretion in CTTSs is highly variable and reinforces the importance of simultaneity in

future multi-instrument/multiwavelength observations of CTTSs. Additionally, we show that each star in our sample exhibits unique relationships between accretion rate and other UV accretion tracers. These empirical relationships should not be utilized when studying individual CTTSs and should be used cautiously for small samples.

Acknowledgments

This work is supported by HST AR-16129 from the Space Telescope Science Institute, which is operated by AURA, Inc. This material is based on work supported by the National Science Foundation under grant No. AST-2108446. This work benefited from discussions with the ODYSSEUS team (https://sites.bu.edu/odysseus/); see Espaillat et al. (2022) for an overview of the ODYSSEUS survey. This work is supported by the ANID FONDECYT Postdoctoral program No. 3220029. We acknowledge support by ANID—Millennium Science Initiative Program—NCN19_171. IM is funded by grant PID2022-138366NA-I00, by the Spanish Ministry of Science and Innovation/State Agency of Research MCIN/AEI/10.13039/501100011033 and the European Union, and by a Ramón y Cajal fellowship RyC2019-026992-I. This work has been supported by the project PRIN-INAF 2019 "Spectroscopically Tracing the Disk Dispersal Evolution (STRADE)" and by the INAF Large Grant 2022 "YSOs Outflow, Disks and Accretion (YODA)." We thank Jerome Bouvier for his suggestions that improved this manuscript. We thank the ULLYSES team at STScI for planning and implementing the HST observations and creating data products, with guidance from the research community.

Facilities: HST, LCOGT, TESS, AAVSO, ASAS-SN, CrAO:Gamma.

Software: Python, Specutils, AstroPy, emcee.

Appendix A
Shock Modeling of RU Lup

As discussed in Section 4.1, our choice of template for RU Lup is complicated by our lack of contemporaneous veiling estimates. The photospheric template we employ in our modeling ($F_{\rm Phot,RU\ Lup}$) is obtained by scaling the raw WTTS spectrum to the radius and distance of RU Lup. While this can introduce additional uncertainty from the stellar radii and distances, we believe that this is a reasonable estimate and is within upper and lower limits for the true photosphere.

As a lower limit on the photospheric contribution ($F_{\rm Phot,Low}$), we can assume that all observed emission originates from accretion by imposing $F_{\rm Phot,Low} = 0$. As an upper limit on the photospheric contribution ($F_{\rm Phot,High}$), we scale the raw WTTS template to the dimmest observation of our V light curve of RU Lup (see Paper II). This assumes that all emission at V originates from the photosphere, implying no contribution from accretion at V. RU Lup is likely accreting at all times, even if only very weakly, meaning that the photospheric contribution to the observed spectrum is likely smaller.

Figure 4 shows the comparison between $F_{\rm Phot,High}$ and $F_{\rm Phot,RU\ Lup}$, along with accretion rates derived using each template. In all cases, the accretion rates obtained using $F_{\rm Phot,RU\ Lup}$ fall between those derived from $F_{\rm Phot,High}$ and $F_{\rm Phot,Low}$.

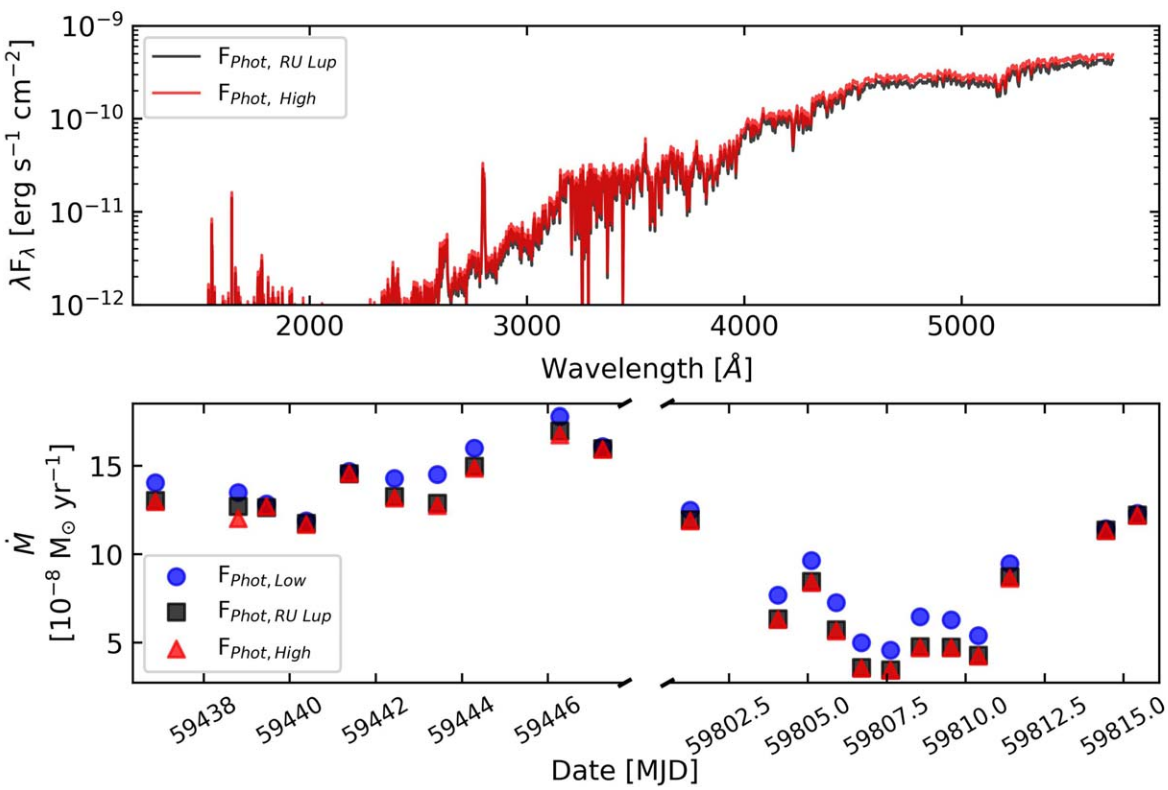

Figure 4. Top: comparison between $F_{\rm Phot,High}$ (red) and $F_{\rm Phot,RU\ Lup}$ (black). Recall that $F_{\rm Phot,Low}$ is zero, i.e., the photosphere does not contribute to the observed spectrum. $F_{\rm Phot,RU\ Lup}$ lays between $F_{\rm Phot,High}$ and $F_{\rm Phot,Low}$. Bottom: accretion rates for RU Lup when using $F_{\rm Phot,High}$ (red triangles), $F_{\rm Phot,RU\ Lup}$ (black squares), and $F_{\rm Phot,Low}$ (blue circles) as photospheric templates.

Appendix B
Effect of No Contemporaneous Photometry on Shock Model Fits

A total of 10 of the 89 HST visits do not have contemporaneous *BgV* photometry. The optical portion of the shock model fit is therefore less constrained, and here we discuss what effect that may have on the results for those visits. To gauge this effect, we rerun our shock models for all visits but remove the photometry, effectively fitting only the UV COS spectrum from ∼1800 to 3200 Å. A comparison between some of the resulting accretion parameters (accretion rate and filling factors) for visits that have contemporaneous photometry is shown in Figure 5.

In general, when no optical photometry is present, the filling factors are accurate to no better than about 50%. Fits without photometry show larger filling factors for the low-density column, with a mean absolute percent error (MAPE) of 4584%. Much of this strong deviation comes from visits that are normally fit with particularly low $f_{\rm Low}$ (near 0%) but jump to the upper limit of $f_{\rm Low}$ = 40% when the photometry is removed. In turn, this higher $f_{\rm Low}$ results in generally lower $f_{\rm Medium}$ (MAPE = 130%). The high-density and very high density columns are generally consistent to within 47% and 263%, respectively, though for the very high density column the strongest deviations occur when $f_{\rm Very\ High}$ is very low and contributes little to the total mass accretion.

While the filling factors are largely inaccurate, the overall mass accretion rate is typically consistent to within about 26%, generally being overestimated owing to the unconstrained $f_{\rm Low}$. These results suggest that while some optical data are very important to constrain the filling factors, the total accretion rate is fairly well constrained. Thus, for visits with no contemporaneous optical photometry (which are noted in Tables 4–5), the accretion rates are likely overestimated by up to about 30%. The associated filling factors are likely inaccurate, with little consistency as to how over/underestimated they are. Figure 6 shows that the correlations between $L_{\rm acc}$ and $L_{\rm Line}$ are largely consistent whether or not visits without contemporaneous photometry are included.

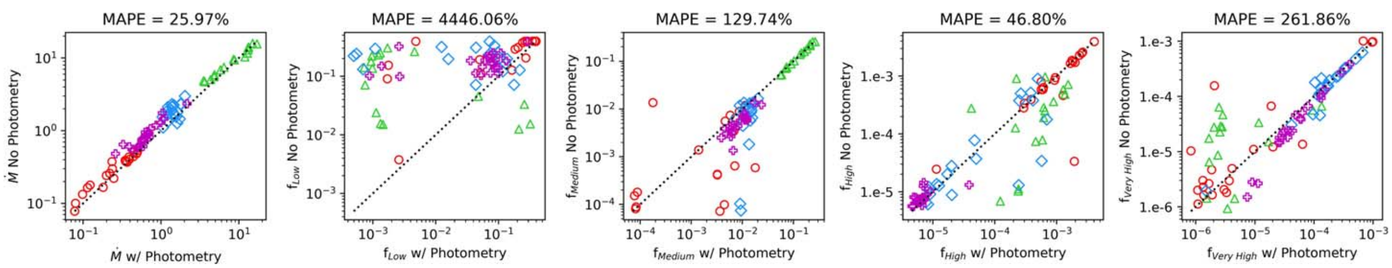

Figure 5. Comparison of accretion shock model results when removing optical photometry points from fitting. Left to right: $\dot{M}$, $f_{\rm Low}$, $f_{\rm Medium}$, $f_{\rm High}$, and $f_{\rm Very\ High}$. Red circles, green triangles, blue diamonds, and purple plus signs represent TW Hya, RU Lup, BP Tau, and GM Aur, respectively. MAPE values between the parameters with and without photometry are listed above each panel.

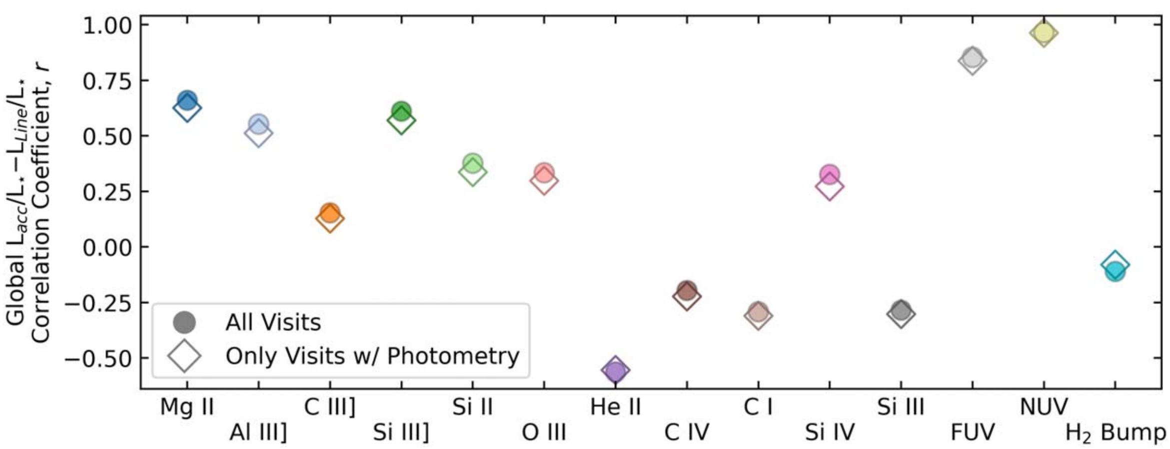

Figure 6. Comparison of $L_{\rm acc}/L_\star$ vs $L_{\rm Line}/L_\star$ correlation coefficients. Filled circles are for all visits, regardless of whether they have contemporaneous optical photometry (what is shown in Figure 3). Open diamonds are for only visits with contemporaneous photometry.

Table 4
Shock Model Results for TW Hya and RU Lup

Object	Visit	Date (MJD)	$\dot{M}$ (10^{-8} $M_\odot$ yr^{-1})	$f_{\rm Low}$ (%)	$f_{\rm Medium}$ (%)	$f_{\rm High}$ (%)	$f_{\rm Very\ High}$ (%)
TW Hya	1.1	59302.69	$0.078^{+0.012}_{-0.007}$	$0.3^{+1.7}_{-0.2}$	$0.9^{+0.05}_{-0.08}$	$0.029^{+0.002}_{-0.006}$	$0.0002^{+0.0011}_{-0.0002}$
TW Hya	1.2	59303.68	$0.25^{+0.04}_{-0.05}$	$27.6^{+3.4}_{-4.1}$	$0.4^{+0.4}_{-0.4}$	$0.05^{+0.04}_{-0.04}$	$0.007^{+0.008}_{-0.007}$
TW Hya	1.3	59304.41	$0.368^{+0.009}_{-0.011}$	$39.5^{+0.4}_{-1.0}$	$0.14^{+0.11}_{-0.08}$	$0.165^{+0.004}_{-0.01}$	$0.0002^{+0.002}_{-0.0002}$
TW Hya	1.4	59305.47	$0.24^{+0.03}_{-0.02}$	$0.8^{+4.6}_{-0.7}$	$1.9^{+0.2}_{-0.2}$	$0.175^{+0.006}_{-0.023}$	$0.0004^{+0.0046}_{-0.0004}$
TW Hya	1.5	59306.53	$0.12^{+0.01}_{-0.01}$	$0.2^{+1.2}_{-0.2}$	$1.27^{+0.08}_{-0.08}$	$0.061^{+0.003}_{-0.015}$	$0.0003^{+0.003}_{-0.0003}$
TW Hya	1.6	59307.19	$0.39^{+0.03}_{-0.04}$	$28.4^{+4.1}_{-4.9}$	$0.7^{+0.3}_{-0.3}$	$0.253^{+0.006}_{-0.008}$	$0.0001^{+0.0013}_{-0.0001}$
TW Hya	1.7	59308.31	$0.22^{+0.02}_{-0.02}$	$21.1^{+3.1}_{-3.5}$	$0.4^{+0.2}_{-0.2}$	$0.095^{+0.003}_{-0.005}$	$0.0001^{+0.0009}_{-0.0001}$
TW Hya	1.8	59309.17	$0.49^{+0.02}_{-0.02}$	$39.4^{+0.4}_{-1.1}$	$1.1^{+0.2}_{-0.1}$	$0.262^{+0.007}_{-0.028}$	$0.0005^{+0.0057}_{-0.0005}$
TW Hya	1.9	59310.56	$0.18^{+0.02}_{-0.02}$	$16.7^{+2.4}_{-2.5}$	$0.6^{+0.1}_{-0.1}$	$0.06^{+0.003}_{-0.005}$	$0.0001^{+0.001}_{-0.0001}$
TW Hya	1.10	59311.56	$0.1^{+0.02}_{-0.02}$	$0.2^{+1.1}_{-0.2}$	$1.2^{+0.1}_{-0.1}$	$0.02^{+0.02}_{-0.02}$	$0.003^{+0.004}_{-0.003}$
TW Hya	1.11	59312.55	$0.08^{+0.02}_{-0.02}$	$5.8^{+2.0}_{-2.0}$	$0.3^{+0.1}_{-0.1}$	$0.039^{+0.003}_{-0.013}$	$0.0004^{+0.0025}_{-0.0003}$
TW Hya	2.1	59668.49	$0.12^{+0.02}_{-0.02}$	$5.5^{+2.3}_{-2.9}$	$0.7^{+0.2}_{-0.1}$	$0.056^{+0.002}_{-0.004}$	$0.0001^{+0.0007}_{-0.0001}$
TW Hya	2.2	59670.61	$0.487^{+0.008}_{-0.007}$	$39.8^{+0.2}_{-0.5}$	$0.74^{+0.06}_{-0.07}$	$0.001^{+0.009}_{-0.001}$	$0.096^{+0.001}_{-0.002}$
TW Hya	2.3	59671.47	$0.2^{+0.02}_{-0.02}$	$18.1^{+2.7}_{-3.0}$	$0.4^{+0.2}_{-0.1}$	$0.092^{+0.003}_{-0.004}$	$0.0001^{+0.0005}_{-0.0001}$
TW Hya	2.4	59673.58	$0.35^{+0.03}_{-0.04}$	$29.3^{+4.5}_{-5.0}$	$0.6^{+0.3}_{-0.3}$	$0.183^{+0.005}_{-0.007}$	$0.0001^{+0.001}_{-0.0001}$
TW Hya	2.5	59674.44	$0.35^{+0.02}_{-0.02}$	$35.1^{+2.2}_{-1.7}$	$0.007^{+0.031}_{-0.005}$	$0.19^{+0.01}_{-0.02}$	$0.003^{+0.005}_{-0.002}$
TW Hya	2.6	59675.77	$0.46^{+0.04}_{-0.06}$	$27.7^{+4.8}_{-7.7}$	$0.3^{+0.5}_{-0.3}$	$0.404^{+0.008}_{-0.012}$	$0.0002^{+0.0013}_{-0.0001}$
TW Hya	2.7	59676.49	$0.39^{+0.01}_{-0.01}$	$37.8^{+1.3}_{-1.5}$	$0.009^{+0.047}_{-0.007}$	$0.233^{+0.006}_{-0.014}$	$0.001^{+0.0032}_{-0.0009}$
TW Hya	2.8	59677.55	$0.51^{+0.02}_{-0.02}$	$39.2^{+0.6}_{-1.2}$	$0.02^{+0.13}_{-0.02}$	$0.19^{+0.01}_{-0.02}$	$0.068^{+0.005}_{-0.004}$
TW Hya	2.9	59678.35	$0.239^{+0.009}_{-0.009}$	$24.4^{+1.1}_{-1.2}$	$0.008^{+0.042}_{-0.006}$	$0.127^{+0.003}_{-0.008}$	$0.0002^{+0.0017}_{-0.0002}$
TW Hya	2.10	59695.41	$0.444^{+0.005}_{-0.006}$	$39.5^{+0.4}_{-0.9}$	$0.008^{+0.032}_{-0.006}$	$0.0007^{+0.003}_{-0.0005}$	$0.099^{+0.001}_{-0.001}$
RU Lup	1.1	59436.88	$13.1^{+0.3}_{-0.3}$	$0.1^{+0.6}_{-0.1}$	$20.5^{+0.4}_{-0.4}$	$0.14^{+0.02}_{-0.02}$	$0.0002^{+0.003}_{-0.0002}$
RU Lup	1.2	59438.80	$12.7^{+0.7}_{-0.9}$	$20.9^{+7.9}_{-10.7}$	$18.2^{+0.7}_{-0.6}$	$0.09^{+0.04}_{-0.08}$	$0.007^{+0.016}_{-0.007}$
RU Lup	1.3	59439.46[a]	$12.6^{+1.2}_{-0.6}$	$3.5^{+18.8}_{-3.4}$	$20.1^{+0.6}_{-0.7}$	$0.07^{+0.03}_{-0.07}$	$0.002^{+0.015}_{-0.002}$
RU Lup	1.4	59440.38[a]	$11.8^{+1.4}_{-0.6}$	$4.5^{+21.7}_{-4.4}$	$18.6^{+0.5}_{-0.7}$	$0.06^{+0.03}_{-0.06}$	$0.001^{+0.012}_{-0.001}$
RU Lup	1.5	59441.38[a]	$14.6^{+0.9}_{-0.6}$	$1.1^{+13.6}_{-1.1}$	$23.6^{+0.6}_{-0.7}$	$0.06^{+0.04}_{-0.06}$	$0.004^{+0.012}_{-0.004}$
RU Lup	1.6	59442.43	$13.3^{+0.3}_{-0.3}$	$0.11^{+0.7}_{-0.09}$	$21.0^{+0.4}_{-0.4}$	$0.13^{+0.02}_{-0.02}$	$0.0002^{+0.0023}_{-0.0002}$
RU Lup	1.7	59443.43	$12.9^{+0.5}_{-0.3}$	$0.5^{+6.0}_{-0.4}$	$21.3^{+0.4}_{-0.4}$	$0.03^{+0.02}_{-0.03}$	$0.002^{+0.006}_{-0.002}$
RU Lup	1.8	59444.29	$15.0^{+0.3}_{-0.3}$	$0.1^{+1.1}_{-0.1}$	$23.5^{+0.5}_{-0.5}$	$0.16^{+0.02}_{-0.02}$	$0.0002^{+0.0028}_{-0.0002}$
RU Lup	1.9	59446.27	$17.0^{+0.4}_{-0.6}$	$19.8^{+3.0}_{-7.7}$	$26.4^{+0.5}_{-0.5}$	$0.008^{+0.026}_{-0.007}$	$0.002^{+0.005}_{-0.001}$
RU Lup	1.10	59447.26[a]	$16.0^{+1.1}_{-0.7}$	$4.4^{+16.6}_{-4.3}$	$25.6^{+0.7}_{-0.9}$	$0.06^{+0.04}_{-0.06}$	$0.004^{+0.013}_{-0.004}$
RU Lup	2.1	59801.26	$12.0^{+0.5}_{-0.5}$	$32.0^{+1.6}_{-3.2}$	$16.1^{+0.4}_{-0.5}$	$0.03^{+0.07}_{-0.03}$	$0.013^{+0.007}_{-0.013}$
RU Lup	2.2	59804.04	$6.4^{+0.1}_{-0.1}$	$0.09^{+0.44}_{-0.07}$	$10.2^{+0.2}_{-0.2}$	$0.049^{+0.008}_{-0.012}$	$0.0002^{+0.0019}_{-0.0002}$
RU Lup	2.3	59805.10	$8.5^{+0.2}_{-0.2}$	$0.09^{+0.59}_{-0.07}$	$13.3^{+0.2}_{-0.3}$	$0.09^{+0.01}_{-0.01}$	$0.0002^{+0.0014}_{-0.0001}$
RU Lup	2.4	59805.90	$5.7^{+0.1}_{-0.1}$	$0.11^{+0.82}_{-0.09}$	$8.9^{+0.2}_{-0.2}$	$0.066^{+0.009}_{-0.009}$	$0.0002^{+0.0013}_{-0.0001}$
RU Lup	2.5	59806.69	$3.6^{+0.2}_{-0.1}$	$0.3^{+2.9}_{-0.3}$	$5.9^{+0.2}_{-0.2}$	$0.014^{+0.009}_{-0.012}$	$0.0004^{+0.0022}_{-0.0004}$
RU Lup	2.6	59807.62	$3.5^{+0.2}_{-0.2}$	$0.2^{+1.4}_{-0.2}$	$5.6^{+0.2}_{-0.2}$	$0.025^{+0.009}_{-0.018}$	$0.0003^{+0.0032}_{-0.0003}$
RU Lup	2.7	59808.55	$4.8^{+0.1}_{-0.1}$	$0.1^{+0.6}_{-0.08}$	$7.3^{+0.2}_{-0.2}$	$0.069^{+0.009}_{-0.009}$	$0.0001^{+0.0011}_{-0.0001}$
RU Lup	2.8	59809.54	$4.8^{+0.1}_{-0.1}$	$0.1^{+0.57}_{-0.08}$	$7.3^{+0.2}_{-0.2}$	$0.064^{+0.007}_{-0.008}$	$0.0001^{+0.001}_{-0.0001}$
RU Lup	2.9	59810.40	$4.3^{+0.1}_{-0.1}$	$0.06^{+0.25}_{-0.04}$	$6.9^{+0.1}_{-0.1}$	$0.026^{+0.006}_{-0.007}$	$0.0002^{+0.0012}_{-0.0001}$
RU Lup	2.10	59811.39	$8.7^{+0.2}_{-0.2}$	$0.06^{+0.3}_{-0.05}$	$14.0^{+0.2}_{-0.3}$	$0.06^{+0.01}_{-0.01}$	$0.0002^{+0.0011}_{-0.0001}$
RU Lup	2.11	59814.43[a]	$11.4^{+1.1}_{-0.6}$	$1.6^{+16.3}_{-1.6}$	$18.0^{+0.6}_{-0.6}$	$0.09^{+0.03}_{-0.09}$	$0.002^{+0.017}_{-0.002}$
RU Lup	2.12	59815.43[a]	$12.2^{+1.2}_{-0.6}$	$1.8^{+19.0}_{-1.8}$	$19.4^{+0.6}_{-0.7}$	$0.09^{+0.03}_{-0.08}$	$0.001^{+0.016}_{-0.001}$

Note.
[a] No contemporaneous photometry.

Table 5
Shock Model Results for BP Tau and GM Aur

Object	Visit	Date (MJD)	$\dot{M}$ (10^{-8} $M_\odot$ yr^{-1})	$f_{\rm Low}$ (%)	$f_{\rm Medium}$ (%)	$f_{\rm High}$ (%)	$f_{\rm Very\ High}$ (%)
BP Tau	1.1	59446.84	$1.86^{+0.09}_{-0.08}$	$1.5^{+1.5}_{-1.1}$	$1.55^{+0.08}_{-0.1}$	$0.0009^{+0.0043}_{-0.0007}$	$0.066^{+0.001}_{-0.001}$
BP Tau	1.2	59448.82[a]	$2.1^{+0.2}_{-0.2}$	$27.8^{+3.3}_{-3.2}$	$0.9^{+0.1}_{-0.1}$	$0.001^{+0.006}_{-0.001}$	$0.0153^{+0.0006}_{-0.0011}$
BP Tau	1.3	59450.81[a]	$3.1^{+0.1}_{-0.2}$	$37.8^{+1.6}_{-3.2}$	$0.88^{+0.12}_{-0.09}$	$0.0011^{+0.0062}_{-0.0008}$	$0.054^{+0.001}_{-0.001}$
BP Tau	1.4	59452.93	$1.19^{+0.09}_{-0.07}$	$1.1^{+1.6}_{-1.0}$	$1.16^{+0.07}_{-0.08}$	$0.0008^{+0.0038}_{-0.0006}$	$0.0365^{+0.0009}_{-0.001}$
BP Tau	1.5	59454.85[a]	$2.7^{+0.2}_{-0.2}$	$33.8^{+3.9}_{-4.4}$	$0.9^{+0.2}_{-0.2}$	$0.001^{+0.01}_{-0.001}$	$0.034^{+0.001}_{-0.002}$
BP Tau	1.6	59457.43	$1.2^{+0.1}_{-0.1}$	$3.5^{+1.0}_{-1.0}$	$1.59^{+0.07}_{-0.15}$	$0.004^{+0.022}_{-0.003}$	$0.0174^{+0.0008}_{-0.0039}$
BP Tau	1.7	59458.95	$1.26^{+0.05}_{-0.06}$	$0.04^{+0.12}_{-0.03}$	$1.24^{+0.07}_{-0.05}$	$0.126^{+0.004}_{-0.01}$	$0.0002^{+0.002}_{-0.0002}$
BP Tau	1.8	59460.87	$1.3^{+0.3}_{-0.2}$	$0.07^{+0.29}_{-0.05}$	$1.6^{+0.2}_{-0.3}$	$0.03^{+0.05}_{-0.02}$	$0.025^{+0.005}_{-0.008}$
BP Tau	1.9	59462.92	$1.31^{+0.05}_{-0.04}$	$0.11^{+0.51}_{-0.09}$	$1.05^{+0.05}_{-0.07}$	$0.001^{+0.007}_{-0.001}$	$0.051^{+0.001}_{-0.002}$
BP Tau	1.10	59464.97	$1.2^{+0.3}_{-0.2}$	$0.04^{+0.12}_{-0.03}$	$1.3^{+0.2}_{-0.3}$	$0.04^{+0.04}_{-0.03}$	$0.019^{+0.005}_{-0.008}$
BP Tau	1.11	59467.09	$1.1^{+0.2}_{-0.2}$	$0.04^{+0.1}_{-0.03}$	$0.9^{+0.2}_{-0.1}$	$0.12^{+0.02}_{-0.03}$	$0.004^{+0.006}_{-0.004}$
BP Tau	1.12	59469.14	$0.91^{+0.06}_{-0.06}$	$2.8^{+0.9}_{-0.9}$	$1.16^{+0.05}_{-0.06}$	$0.0011^{+0.0056}_{-0.0009}$	$0.0123^{+0.0004}_{-0.001}$
BP Tau	2.1	59926.16	$1.3^{+0.3}_{-0.3}$	$7.5^{+1.2}_{-1.2}$	$1.4^{+0.2}_{-0.3}$	$0.03^{+0.05}_{-0.03}$	$0.009^{+0.005}_{-0.009}$
BP Tau	2.2	59928.47	$1.4^{+0.3}_{-0.3}$	$6.2^{+1.2}_{-1.3}$	$1.1^{+0.3}_{-0.2}$	$0.09^{+0.03}_{-0.04}$	$0.006^{+0.008}_{-0.006}$
BP Tau	2.3	59930.06	$1.11^{+0.06}_{-0.06}$	$9.5^{+1.0}_{-0.9}$	$0.83^{+0.06}_{-0.05}$	$0.044^{+0.002}_{-0.005}$	$0.0001^{+0.0009}_{-0.0001}$
BP Tau	2.4	59932.57	$1.12^{+0.04}_{-0.04}$	$0.04^{+0.12}_{-0.03}$	$0.9^{+0.06}_{-0.05}$	$0.132^{+0.004}_{-0.007}$	$0.0002^{+0.0012}_{-0.0001}$
BP Tau	2.5	59936.54[a]	$1.7^{+0.3}_{-0.3}$	$5.0^{+4.4}_{-4.3}$	$1.1^{+0.3}_{-0.2}$	$0.164^{+0.009}_{-0.05}$	$0.001^{+0.009}_{-0.001}$
BP Tau	2.6	59938.52	$1.4^{+0.2}_{-0.2}$	$12.0^{+1.3}_{-1.4}$	$1.2^{+0.2}_{-0.2}$	$0.03^{+0.02}_{-0.03}$	$0.004^{+0.005}_{-0.004}$
BP Tau	2.7	59940.70	$0.9^{+0.1}_{-0.2}$	$0.2^{+0.7}_{-0.2}$	$1.0^{+0.2}_{-0.1}$	$0.07^{+0.01}_{-0.03}$	$0.003^{+0.005}_{-0.003}$
BP Tau	2.8	59942.55	$1.44^{+0.09}_{-0.08}$	$8.0^{+1.4}_{-1.3}$	$1.53^{+0.07}_{-0.09}$	$0.001^{+0.009}_{-0.001}$	$0.0174^{+0.0006}_{-0.0015}$
BP Tau	2.9	59944.67	$1.6^{+0.3}_{-0.3}$	$0.11^{+0.58}_{-0.09}$	$1.6^{+0.2}_{-0.3}$	$0.12^{+0.04}_{-0.04}$	$0.015^{+0.007}_{-0.008}$
BP Tau	2.10	59946.58	$1.57^{+0.1}_{-0.09}$	$16.4^{+1.3}_{-1.3}$	$1.07^{+0.07}_{-0.1}$	$0.002^{+0.013}_{-0.002}$	$0.0138^{+0.0007}_{-0.0023}$
BP Tau	2.11	59948.63	$1.4^{+0.3}_{-0.3}$	$7.1^{+1.5}_{-1.5}$	$1.1^{+0.3}_{-0.3}$	$0.07^{+0.05}_{-0.04}$	$0.01^{+0.008}_{-0.008}$
BP Tau	2.12	59950.48	$1.6^{+0.4}_{-0.5}$	$5.7^{+1.6}_{-2.1}$	$1.5^{+0.16}_{-0.2}$	$0.11^{+0.02}_{-0.09}$	$0.004^{+0.016}_{-0.004}$
GM Aur	1.1	59500.52	$0.49^{+0.04}_{-0.04}$	$7.2^{+0.9}_{-0.9}$	$0.59^{+0.04}_{-0.04}$	$0.0007^{+0.0025}_{-0.0005}$	$0.0008^{+0.0003}_{-0.0005}$
GM Aur	1.2	59502.30	$0.86^{+0.05}_{-0.05}$	$7.2^{+1.1}_{-1.1}$	$1.14^{+0.05}_{-0.06}$	$0.0007^{+0.0031}_{-0.0005}$	$0.0152^{+0.0004}_{-0.0007}$
GM Aur	1.3	59503.69	$0.58^{+0.03}_{-0.03}$	$9.5^{+0.8}_{-0.8}$	$0.46^{+0.03}_{-0.04}$	$0.0006^{+0.0022}_{-0.0004}$	$0.0049^{+0.0003}_{-0.0004}$
GM Aur	1.4	59504.88	$0.43^{+0.03}_{-0.03}$	$5.1^{+0.7}_{-0.7}$	$0.58^{+0.03}_{-0.03}$	$0.0005^{+0.0014}_{-0.0003}$	$0.0026^{+0.0002}_{-0.0003}$
GM Aur	1.5	59506.67	$0.58^{+0.04}_{-0.04}$	$3.6^{+0.8}_{-0.8}$	$1.11^{+0.04}_{-0.05}$	$0.0007^{+0.0036}_{-0.0006}$	$0.003^{+0.0003}_{-0.0006}$
GM Aur	1.6	59507.93	$1.04^{+0.03}_{-0.02}$	$0.1^{+0.6}_{-0.1}$	$2.38^{+0.04}_{-0.05}$	$0.0007^{+0.0034}_{-0.0006}$	$0.0132^{+0.0005}_{-0.0007}$
GM Aur	1.7	59509.65	$2.15^{+0.08}_{-0.08}$	$28.6^{+1.8}_{-1.8}$	$1.7^{+0.1}_{-0.1}$	$0.0008^{+0.0043}_{-0.0006}$	$0.04^{+0.001}_{-0.001}$
GM Aur	1.8	59554.32	$0.26^{+0.03}_{-0.02}$	$0.07^{+0.27}_{-0.05}$	$0.61^{+0.03}_{-0.04}$	$0.004^{+0.007}_{-0.004}$	$0.0013^{+0.0007}_{-0.0013}$
GM Aur	1.9	59557.17	$0.96^{+0.06}_{-0.06}$	$9.8^{+1.3}_{-1.3}$	$1.21^{+0.06}_{-0.07}$	$0.0009^{+0.0054}_{-0.0007}$	$0.013^{+0.0006}_{-0.001}$
GM Aur	1.10	59558.69	$0.39^{+0.03}_{-0.02}$	$0.2^{+0.7}_{-0.1}$	$0.92^{+0.03}_{-0.04}$	$0.0006^{+0.0023}_{-0.0005}$	$0.0037^{+0.0003}_{-0.0005}$
GM Aur	1.11	59560.21	$0.32^{+0.02}_{-0.01}$	$0.1^{+0.37}_{-0.08}$	$0.68^{+0.02}_{-0.03}$	$0.0007^{+0.0031}_{-0.0006}$	$0.006^{+0.0003}_{-0.0006}$
GM Aur	2.1	59909.89	$0.51^{+0.04}_{-0.04}$	$9.5^{+1.0}_{-1.1}$	$0.4^{+0.04}_{-0.04}$	$0.0007^{+0.0029}_{-0.0005}$	$0.001^{+0.0003}_{-0.0005}$
GM Aur	2.2	59911.41	$0.55^{+0.05}_{-0.04}$	$8.0^{+1.1}_{-1.1}$	$0.62^{+0.05}_{-0.05}$	$0.0006^{+0.0019}_{-0.0004}$	$0.0026^{+0.0003}_{-0.0004}$
GM Aur	2.3	59912.80	$1.07^{+0.05}_{-0.06}$	$7.5^{+1.2}_{-1.3}$	$1.25^{+0.07}_{-0.07}$	$0.0007^{+0.0031}_{-0.0005}$	$0.0293^{+0.0007}_{-0.0008}$
GM Aur	2.4	59914.39	$0.57^{+0.05}_{-0.05}$	$7.3^{+1.1}_{-1.1}$	$0.73^{+0.05}_{-0.05}$	$0.0006^{+0.0025}_{-0.0005}$	$0.0027^{+0.0003}_{-0.0005}$
GM Aur	2.5	59915.78	$0.69^{+0.06}_{-0.06}$	$8.4^{+1.4}_{-1.3}$	$0.83^{+0.06}_{-0.07}$	$0.0006^{+0.0029}_{-0.0005}$	$0.0064^{+0.0004}_{-0.0006}$
GM Aur	2.6	59917.30	$0.71^{+0.05}_{-0.05}$	$6.0^{+1.3}_{-1.3}$	$1.19^{+0.06}_{-0.06}$	$0.0007^{+0.0034}_{-0.0006}$	$0.0044^{+0.0004}_{-0.0006}$
GM Aur	2.7	59919.29	$0.69^{+0.03}_{-0.03}$	$5.2^{+0.8}_{-0.8}$	$1.1^{+0.04}_{-0.04}$	$0.0005^{+0.0018}_{-0.0004}$	$0.008^{+0.0003}_{-0.0004}$
GM Aur	2.8	59920.34	$0.6^{+0.03}_{-0.03}$	$8.6^{+0.8}_{-0.8}$	$0.67^{+0.03}_{-0.03}$	$0.0004^{+0.0013}_{-0.0003}$	$0.003^{+0.0002}_{-0.0003}$
GM Aur	2.9	59922.33	$0.69^{+0.05}_{-0.05}$	$12.7^{+1.1}_{-1.2}$	$0.5^{+0.05}_{-0.05}$	$0.0005^{+0.0015}_{-0.0003}$	$0.0031^{+0.0003}_{-0.0003}$
GM Aur	2.10	59923.52	$0.67^{+0.04}_{-0.04}$	$5.8^{+0.9}_{-0.9}$	$1.12^{+0.04}_{-0.04}$	$0.0005^{+0.0017}_{-0.0004}$	$0.0036^{+0.0003}_{-0.0003}$
GM Aur	2.11	59925.17	$0.62^{+0.04}_{-0.04}$	$3.3^{+1.0}_{-1.0}$	$1.17^{+0.04}_{-0.05}$	$0.0006^{+0.0024}_{-0.0004}$	$0.0059^{+0.0003}_{-0.0004}$

Note.
[a] No contemporaneous photometry.

Appendix C
Shock Model Results

Tables 4 and 5 show the mass accretion rates and filling factors of the four accretion columns obtained from our shock model fitting of TW Hya, RU Lup, BP Tau, and GM Aur. Figures 7–14 show the shock model fits for each HST visit.

For TW Hya, BP Tau, and GM Aur, the upper/lower uncertainties are the average differences between the 84th/16th and 50th percentiles in the resulting posterior distributions, except where the standard deviation of results from all $F_{\rm Phot,True}$ is larger. For RU Lup, we only cite the difference between the 84th/16th and 50th percentiles in the resulting posterior distributions, as only one $F_{\rm Phot,True}$ was used. These uncertainties thus underestimate the true uncertainty in the model parameters given the uncertainty in the true, underlying $F_{\rm Phot,True}$. Additionally, the uncertainties for all four targets only describe the widths of the posterior distributions of each parameter. They do not properly account for nonsystematic uncertainties, such as R_*, M_*, and A_V. RE19 note that the true uncertainties are likely to be at least 10% when accounting for other sources of error.

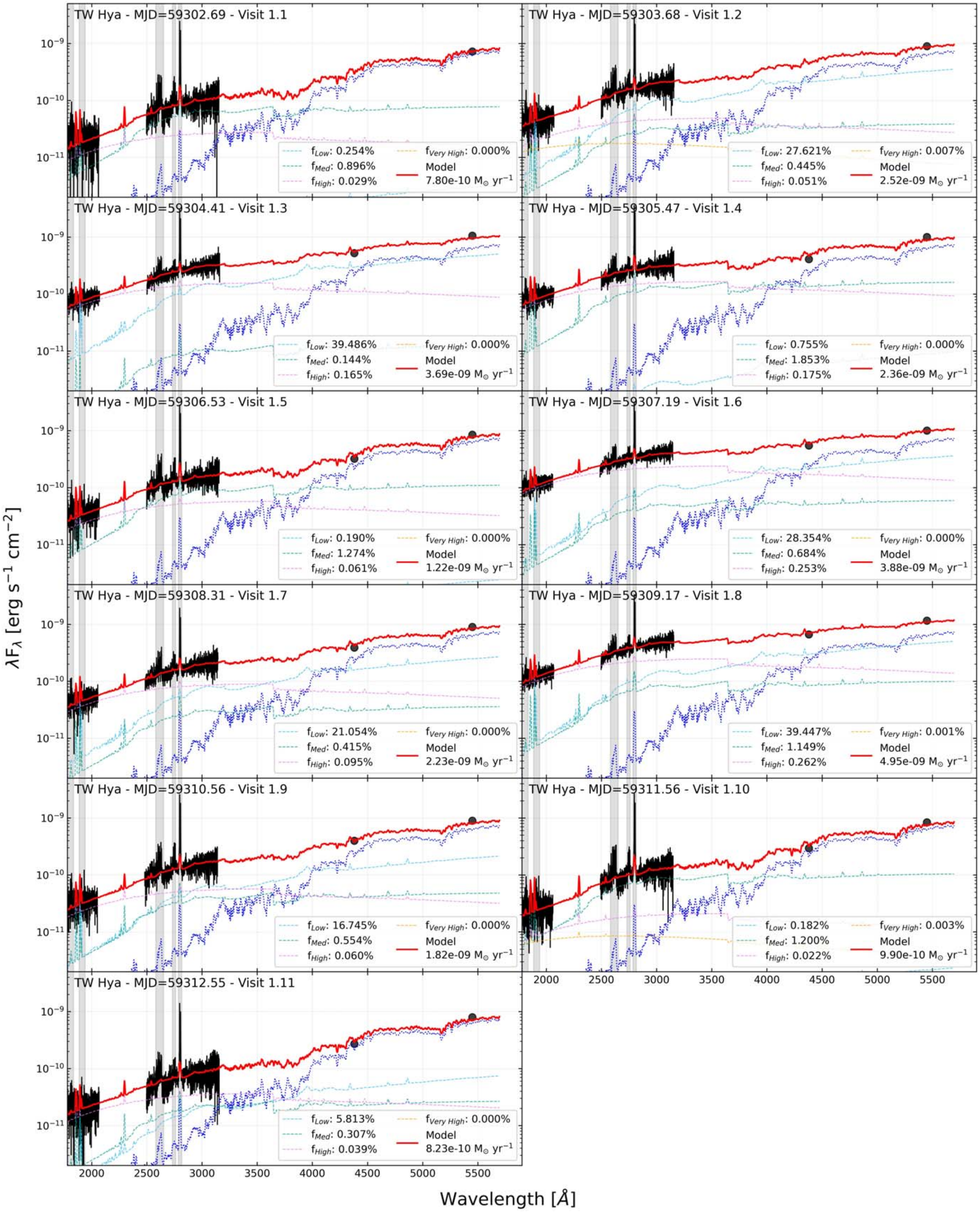

Figure 7. Shock model fits for TW Hya, Epoch 1. Black, red, and dotted blue lines are the data, total model, and scaled WTTS template ($F_{\mathrm{Phot,Obs}}$), respectively. Black circles are contemporaneous photometry points. Cyan, green, pink, and orange lines represent the low-, medium-, high-, and very high-density accretion columns, respectively. In some cases the contribution from an individual column is low and does not appear in the plot. Filled gray regions are masked in the fitting owing to the presence of bright emission lines.

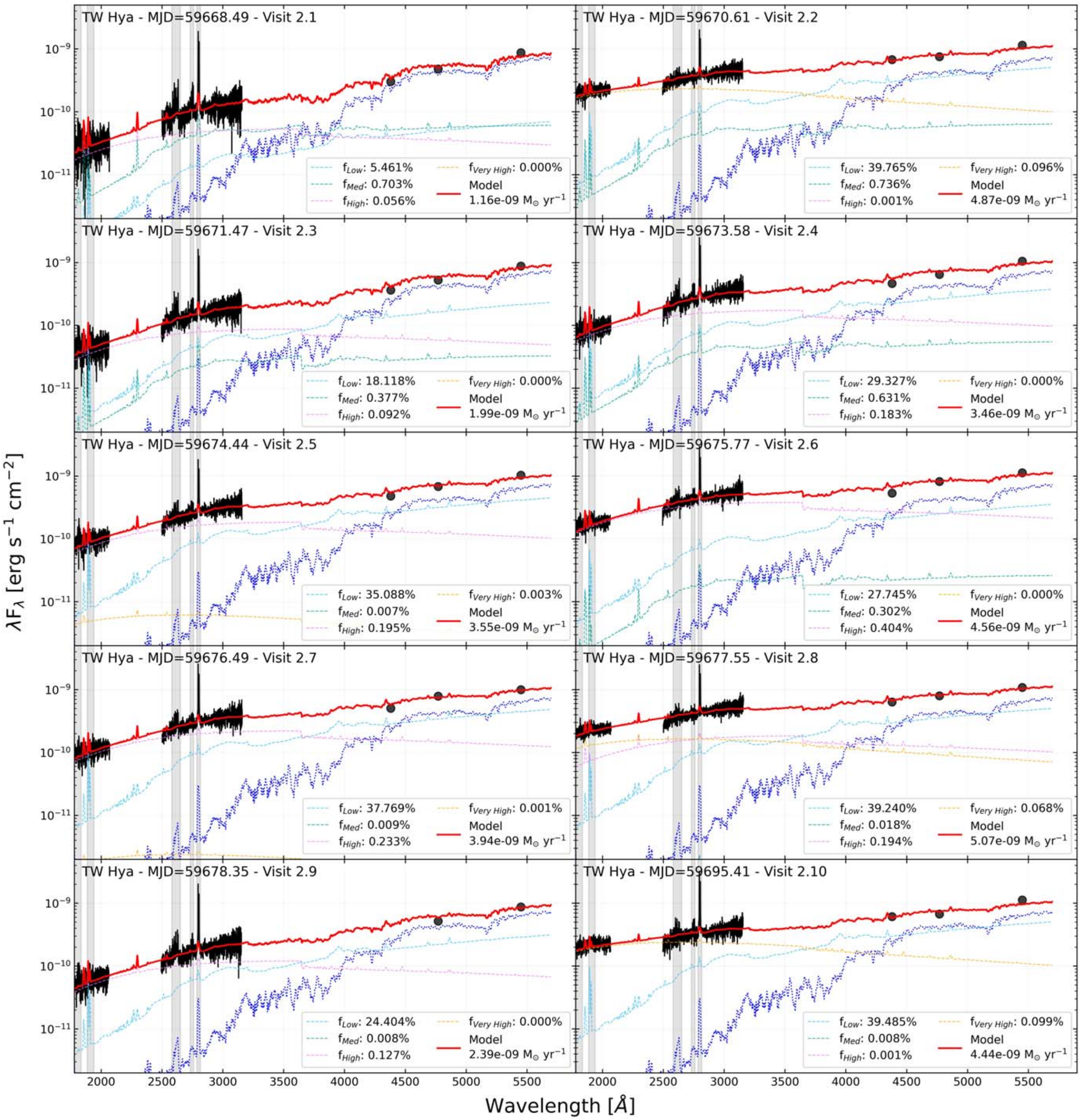

Figure 8. Same as Figure 7, but for TW Hya, Epoch 2.

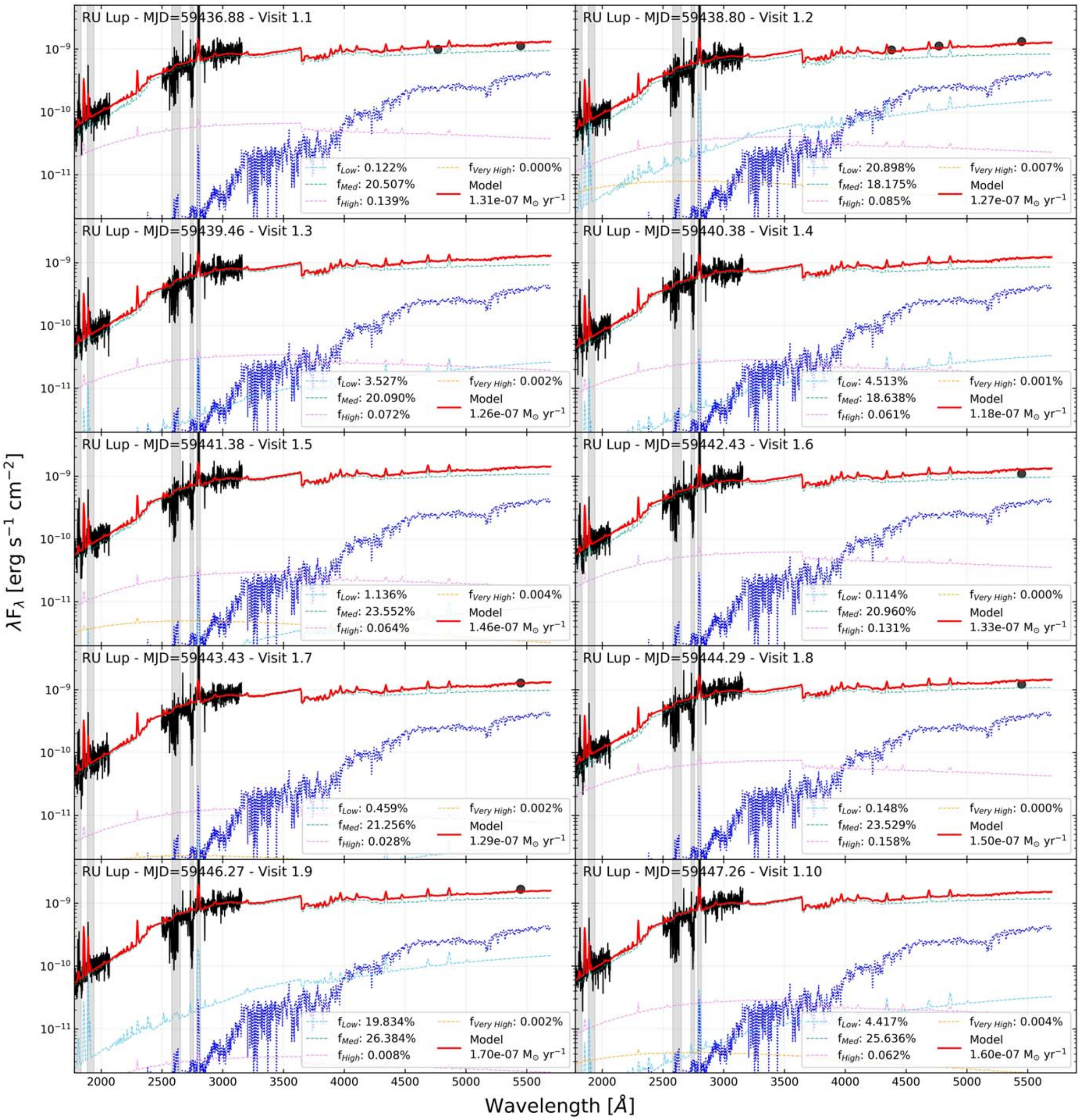

Figure 9. Same as Figure 7, but for RU Lup, Epoch 1.

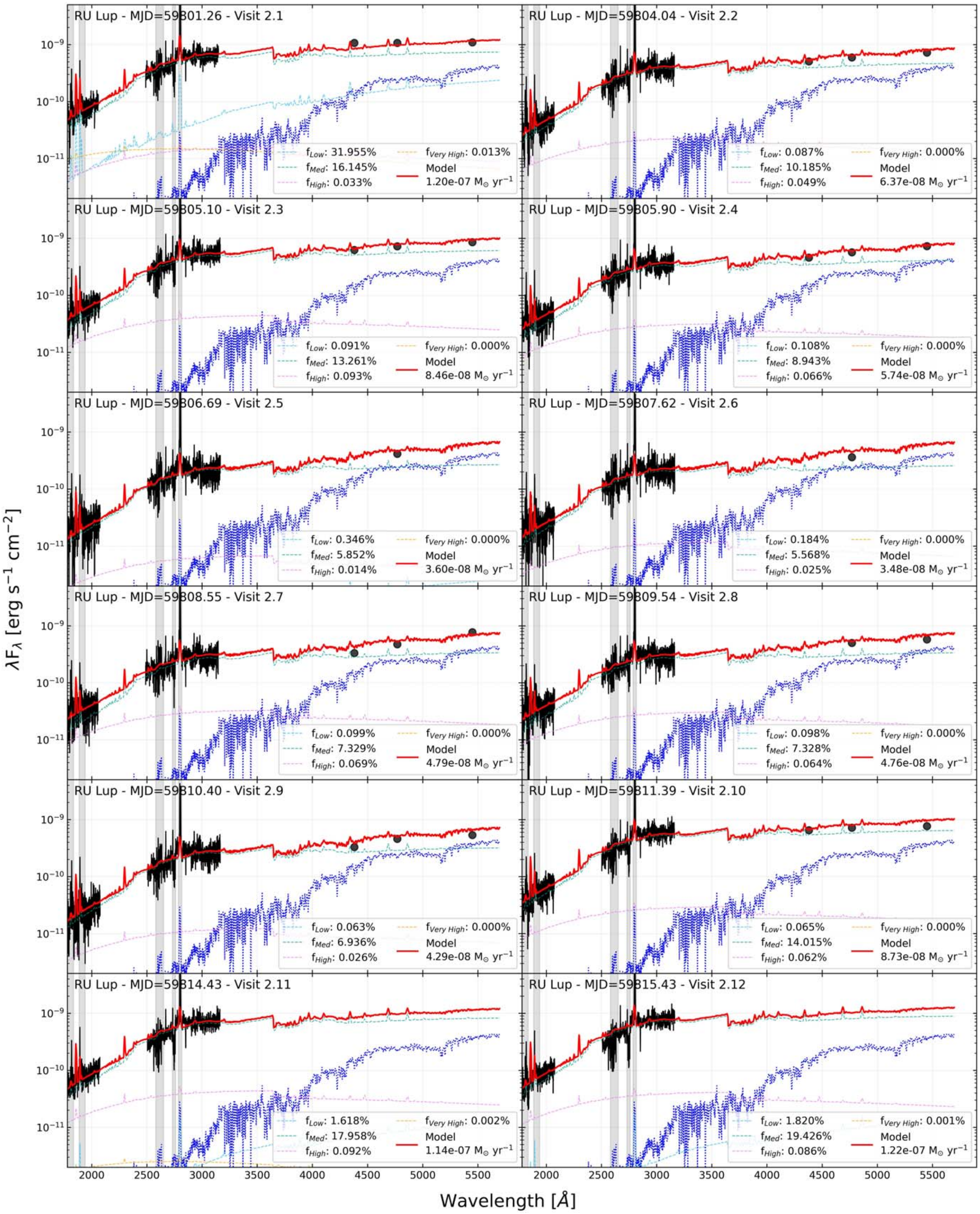

Figure 10. Same as Figure 7, but for RU Lup, Epoch 2.

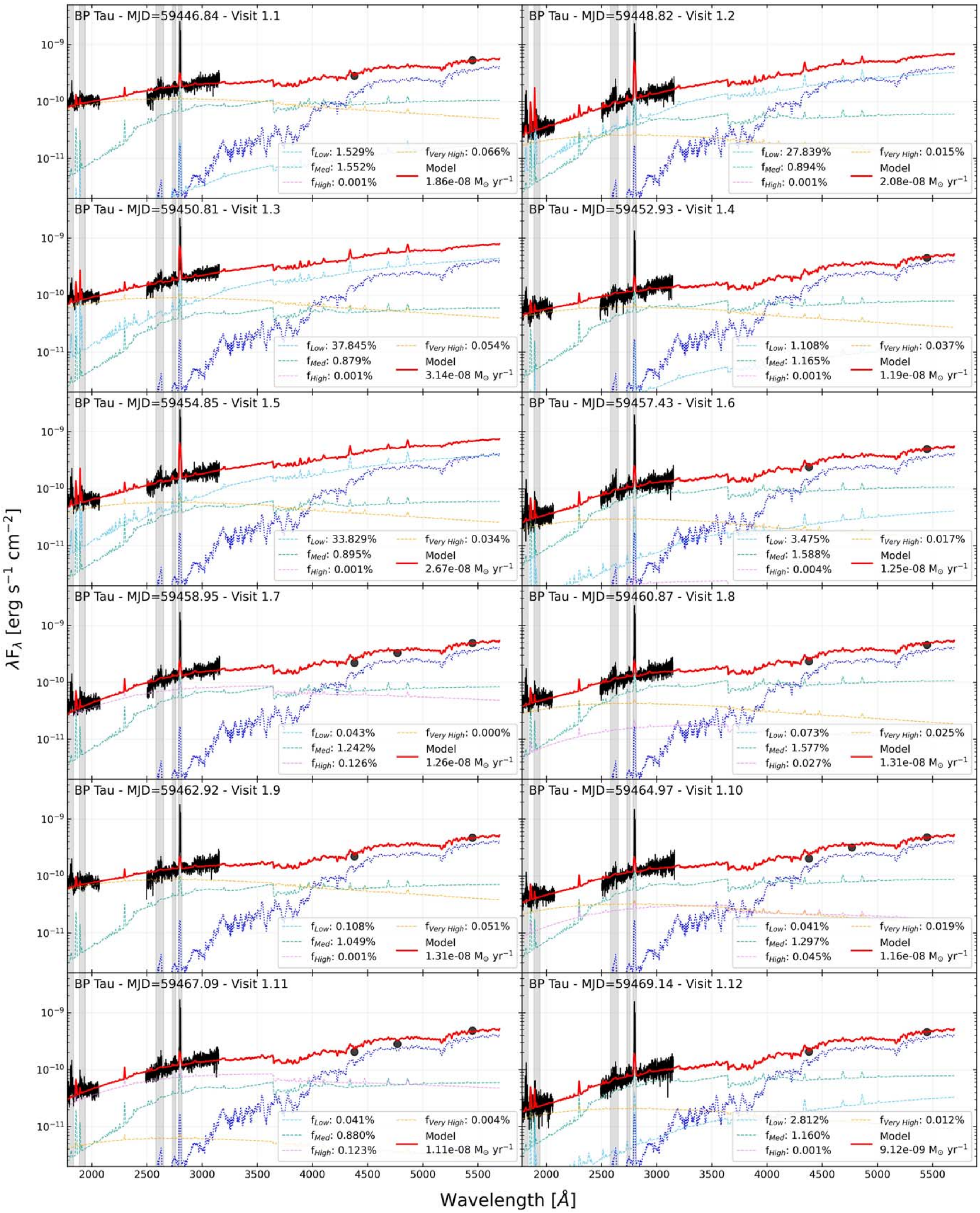

Figure 11. Same as Figure 7, but for BP Tau, Epoch 1.

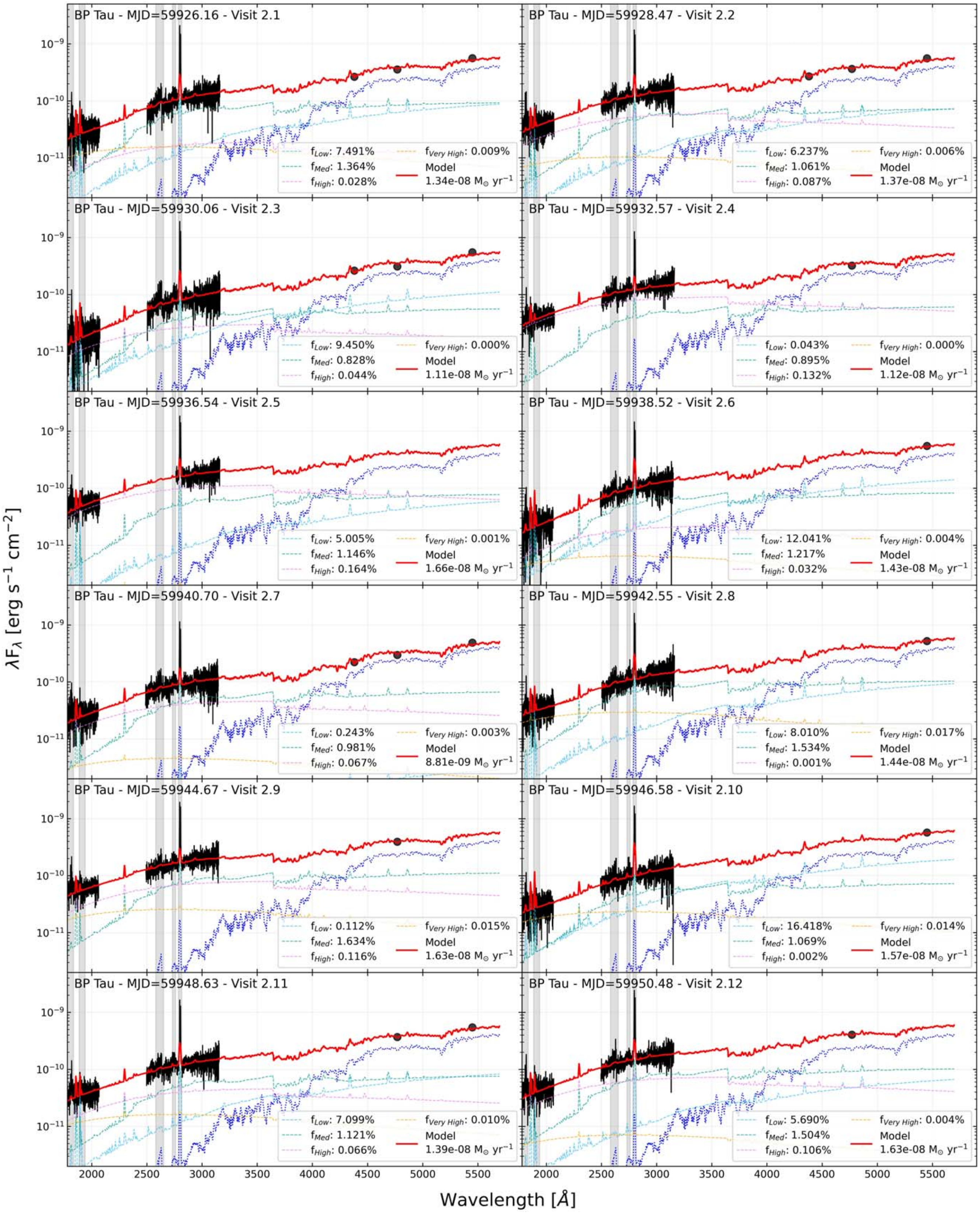

Figure 12. Same as Figure 7, but for BP Tau, Epoch 2.

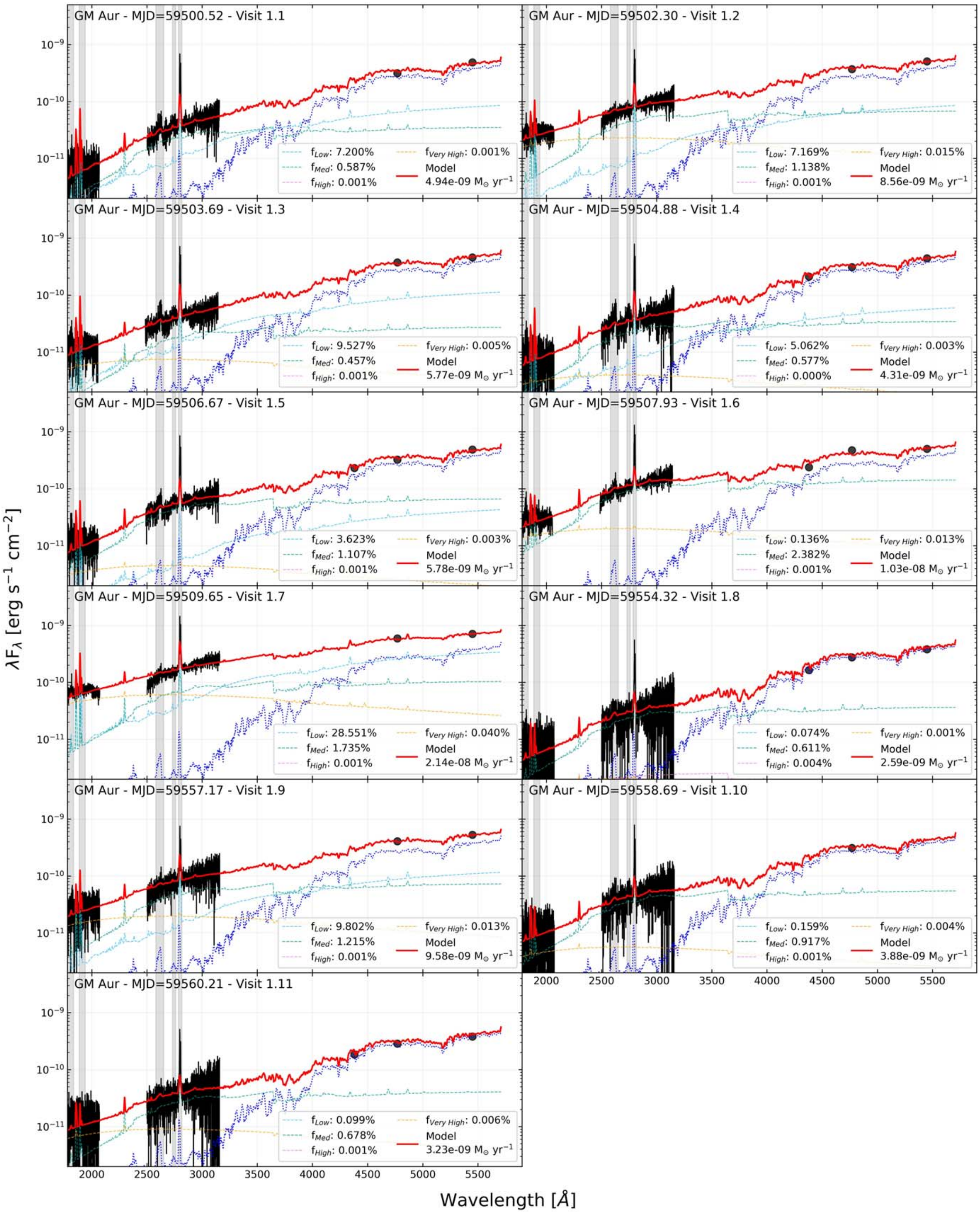

Figure 13. Same as Figure 7, but for GM Aur, Epoch 1.

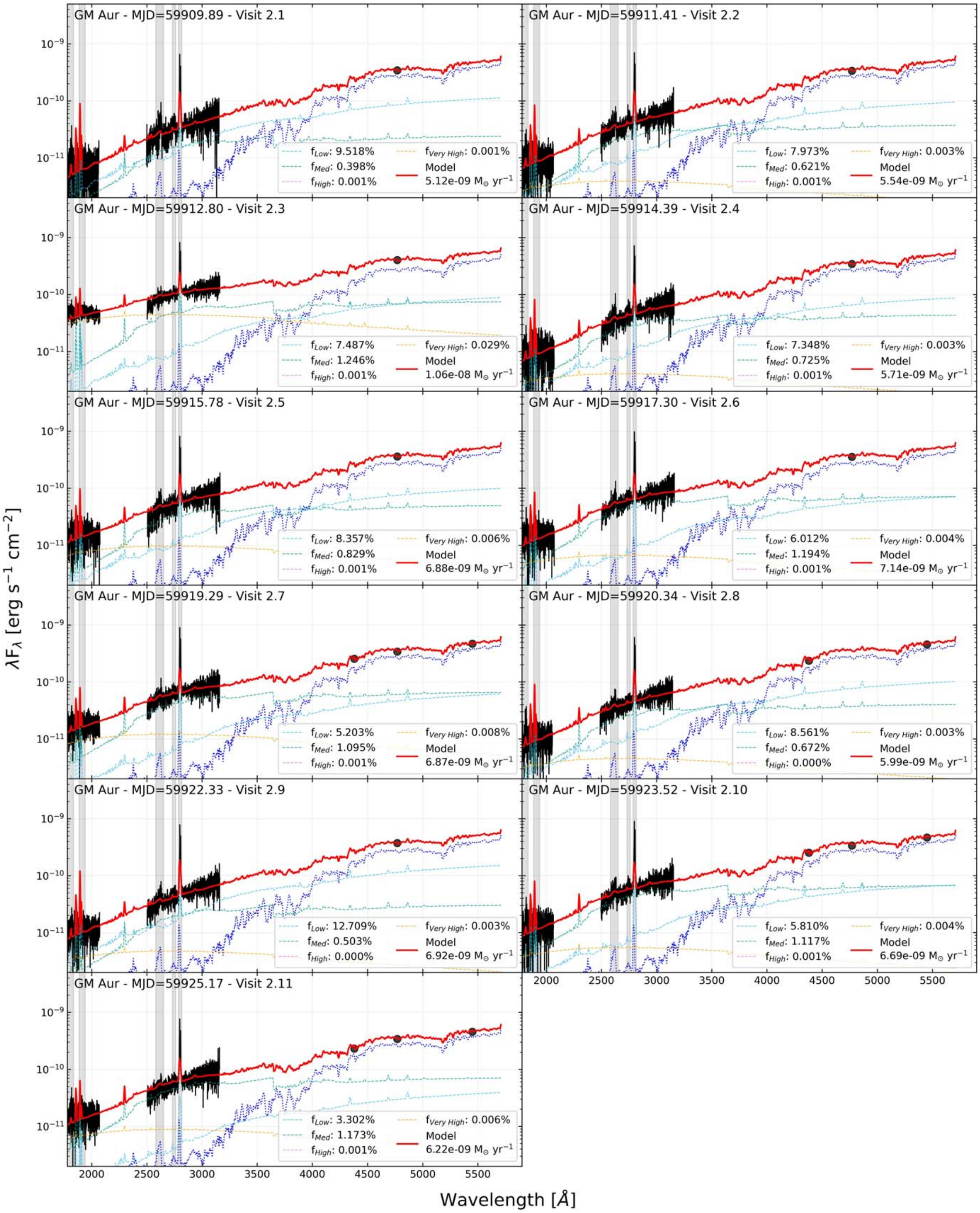

Figure 14. Same as Figure 7, but for GM Aur, Epoch 2.

Appendix D
UV Luminosities

Given in Tables 6–9 are the UV feature luminosities, including 11 FUV–NUV lines, FUV/NUV continua, and the H_2 bump. Table 10 gives the log–log linear fit and Spearman correlation coefficients between $L_{\rm acc}$ and $L_{\rm UV}$ for each UV feature.

Table 6
UV Line, FUV/NUV Continuum, and H_2 Bump Luminosities for TW Hya in Units of 10^{29} erg s^{-1}

Object	Visit	Si III	Si IV	C I	C IV	He II	O III]	Si II	Si III]	C III]	Al III]	Mg II	FUV	NUV	Bump
TW Hya	1.1	3.2 ± 0.1	4.3 ± 0.1	2.4 ± 0.1	37.6 ± 0.3	21.6 ± 0.3	0.3 ± 0.1	1.3 ± 0.4	0.8 ± 0.3	1.0 ± 0.3	2.4 ± 0.3	83.8 ± 1.5	40.9 ± 0.1	83.1 ± 0.2	3.5 ± 0.4
TW Hya	1.2	3.7 ± 0.1	5.3 ± 0.1	2.8 ± 0.1	47.9 ± 0.3	24.4 ± 0.3	0.5 ± 0.1	1.4 ± 0.4	1.2 ± 0.3	2.0 ± 0.4	2.8 ± 0.6	117.0 ± 1.8	73.3 ± 0.2	165.0 ± 0.4	4.3 ± 0.4
TW Hya	1.3	3.1 ± 0.1	6.4 ± 0.1	3.2 ± 0.1	93.7 ± 0.4	32.8 ± 0.4	0.9 ± 0.1	2.4 ± 0.6	1.2 ± 0.5	1.6 ± 0.5	1.3 ± 0.6	109.0 ± 1.7	115.0 ± 0.3	261.0 ± 0.6	6.7 ± 0.7
TW Hya	1.4	3.0 ± 0.1	5.2 ± 0.1	2.7 ± 0.1	64.6 ± 0.3	27.4 ± 0.3	0.7 ± 0.1	3.1 ± 0.6	1.4 ± 0.6	0.3 ± 0.5	1.7 ± 0.8	141.0 ± 2.3	128.0 ± 0.3	268.0 ± 0.7	5.4 ± 0.6
TW Hya	1.5	3.3 ± 0.1	6.1 ± 0.1	3.0 ± 0.1	57.1 ± 0.4	27.2 ± 0.3	0.5 ± 0.1	1.4 ± 0.4	1.7 ± 0.4	1.7 ± 0.4	2.2 ± 0.5	104.0 ± 1.5	63.8 ± 0.2	135.0 ± 0.3	4.3 ± 0.4
TW Hya	1.6	4.0 ± 0.1	6.3 ± 0.1	3.0 ± 0.1	96.0 ± 0.4	39.4 ± 0.3	0.8 ± 0.1	0.3 ± 0.5	1.0 ± 0.6	2.1 ± 0.5	1.5 ± 0.8	110.0 ± 2.1	158.0 ± 0.4	343.0 ± 0.8	7.9 ± 0.8
TW Hya	1.7	4.2 ± 0.1	5.6 ± 0.1	3.2 ± 0.1	69.5 ± 0.4	35.5 ± 0.4	0.4 ± 0.1	1.7 ± 0.4	0.2 ± 0.3	1.5 ± 0.4	1.7 ± 0.6	68.5 ± 1.4	79.1 ± 0.2	169.0 ± 0.4	5.2 ± 0.5
TW Hya	1.8	4.3 ± 0.1	7.3 ± 0.1	3.7 ± 0.1	131.0 ± 0.5	49.0 ± 0.4	1.0 ± 0.1	2.4 ± 0.7	1.8 ± 0.5	1.7 ± 0.6	2.4 ± 0.7	123.0 ± 1.7	176.0 ± 0.4	407.0 ± 1.1	7.4 ± 0.8
TW Hya	1.9	4.5 ± 0.1	6.4 ± 0.1	3.6 ± 0.1	74.6 ± 0.4	31.7 ± 0.3	0.6 ± 0.1	1.6 ± 0.3	0.9 ± 0.3	1.7 ± 0.3	1.9 ± 0.5	89.6 ± 1.1	66.9 ± 0.2	131.0 ± 0.3	5.7 ± 0.6
TW Hya	1.10	4.0 ± 0.1	5.6 ± 0.1	3.2 ± 0.1	43.7 ± 0.2	18.9 ± 0.3	0.6 ± 0.1	1.0 ± 0.4	0.4 ± 0.3	2.3 ± 0.4	0.7 ± 0.5	100.0 ± 1.6	49.0 ± 0.1	106.0 ± 0.3	5.2 ± 0.5
TW Hya	1.11	3.6 ± 0.1	5.1 ± 0.1	2.8 ± 0.1	33.5 ± 0.2	20.3 ± 0.3	0.3 ± 0.1	0.8 ± 0.3	0.4 ± 0.2	1.1 ± 0.3	1.1 ± 0.3	57.3 ± 1.1	42.7 ± 0.1	70.5 ± 0.2	4.6 ± 0.5
TW Hya	2.1	3.9 ± 0.1	5.2 ± 0.1	3.3 ± 0.1	58.8 ± 0.4	29.3 ± 0.4	0.3 ± 0.1	0.4 ± 0.3	−0.0 ± 0.3	0.8 ± 0.3	1.3 ± 0.5	65.7 ± 1.3	59.1 ± 0.2	109.0 ± 0.3	5.8 ± 0.6
TW Hya	2.2	4.1 ± 0.1	5.6 ± 0.1	3.2 ± 0.1	81.2 ± 0.5	36.7 ± 0.5	0.7 ± 0.2	0.1 ± 0.8	0.6 ± 0.7	1.1 ± 0.8	−0.0 ± 0.7	49.1 ± 1.5	301.0 ± 0.7	385.0 ± 1.0	6.6 ± 0.7
TW Hya	2.3	3.5 ± 0.1	5.0 ± 0.1	3.1 ± 0.1	65.4 ± 0.4	31.1 ± 0.5	0.4 ± 0.1	1.5 ± 0.4	0.9 ± 0.3	1.2 ± 0.4	1.2 ± 0.5	56.7 ± 1.2	75.5 ± 0.2	159.0 ± 0.4	5.3 ± 0.5
TW Hya	2.4	3.5 ± 0.1	6.2 ± 0.1	3.3 ± 0.1	134.0 ± 0.5	47.0 ± 0.4	0.7 ± 0.1	0.9 ± 0.4	1.1 ± 0.5	2.2 ± 0.5	3.7 ± 0.7	86.4 ± 1.5	126.0 ± 0.3	283.0 ± 0.7	7.7 ± 0.8
TW Hya	2.5	4.0 ± 0.1	6.5 ± 0.1	3.6 ± 0.1	102.0 ± 0.5	49.5 ± 0.6	0.8 ± 0.1	1.3 ± 0.6	1.1 ± 0.5	0.8 ± 0.5	0.9 ± 0.5	57.8 ± 1.8	145.0 ± 0.4	274.0 ± 0.7	7.3 ± 0.7
TW Hya	2.6	3.3 ± 0.1	5.2 ± 0.1	3.3 ± 0.1	108.0 ± 0.6	51.2 ± 0.6	0.8 ± 0.2	1.7 ± 0.7	0.9 ± 0.7	2.3 ± 0.7	0.4 ± 0.8	84.4 ± 1.9	253.0 ± 0.6	453.0 ± 1.1	5.3 ± 0.6
TW Hya	2.7	3.8 ± 0.1	5.6 ± 0.1	3.2 ± 0.1	90.2 ± 0.5	41.8 ± 0.5	0.7 ± 0.1	2.3 ± 0.5	0.7 ± 0.5	1.6 ± 0.6	3.0 ± 0.7	82.1 ± 1.8	157.0 ± 0.4	311.0 ± 0.7	5.4 ± 0.6
TW Hya	2.8	3.9 ± 0.1	6.5 ± 0.1	3.7 ± 0.1	100.0 ± 0.5	45.5 ± 0.6	0.9 ± 0.2	0.7 ± 0.8	1.1 ± 0.6	1.2 ± 0.7	−0.0 ± 0.8	66.2 ± 1.9	319.0 ± 0.8	448.0 ± 1.2	6.8 ± 0.7
TW Hya	2.9	3.6 ± 0.1	5.6 ± 0.1	3.4 ± 0.1	68.6 ± 0.5	34.5 ± 0.5	0.5 ± 0.1	0.9 ± 0.4	0.9 ± 0.4	0.7 ± 0.4	2.0 ± 0.5	65.6 ± 1.4	94.0 ± 0.2	186.0 ± 0.5	6.3 ± 0.6
TW Hya	2.10	4.1 ± 0.1	6.6 ± 0.1	3.5 ± 0.1	78.5 ± 0.4	39.8 ± 0.5	0.2 ± 0.2	0.4 ± 0.7	2.4 ± 0.8	1.4 ± 0.8	−1.6 ± 0.8	111.0 ± 1.7	317.0 ± 0.8	346.0 ± 0.9	9.4 ± 1.0

Table 7
Same as Table 6, but for RU Lup

Object	Visit	Si III	Si IV	C I	C IV	He II	O III	Si II	Si III]	C III]	Al III]	Mg II	FUV	NUV	Bump
RU Lup	1.1	0.7 ± 0.0	7.8 ± 0.1	0.5 ± 0.0	12.7 ± 0.2	1.6 ± 0.1	1.1 ± 0.1	3.5 ± 0.6	18.1 ± 0.8	0.8 ± 0.4	30.7 ± 1.2	338.0 ± 2.6	523.0 ± 1.5	4670.0 ± 12.8	3.1 ± 0.6
RU Lup	1.2	0.6 ± 0.0	8.1 ± 0.1	0.5 ± 0.0	14.9 ± 0.2	1.8 ± 0.1	1.3 ± 0.1	2.7 ± 0.5	12.8 ± 0.8	0.5 ± 0.5	23.3 ± 0.9	289.0 ± 2.8	501.0 ± 1.4	3890.0 ± 10.1	4.6 ± 1.0
RU Lup	1.3	0.6 ± 0.0	8.9 ± 0.1	0.5 ± 0.0	16.5 ± 0.2	2.3 ± 0.2	1.3 ± 0.1	8.6 ± 0.8	17.5 ± 1.0	1.9 ± 0.5	24.6 ± 1.2	314.0 ± 2.5	521.0 ± 1.4	4250.0 ± 11.1	7.0 ± 1.4
RU Lup	1.4	0.7 ± 0.0	8.8 ± 0.1	0.5 ± 0.0	17.3 ± 0.2	2.0 ± 0.1	1.2 ± 0.1	6.7 ± 0.7	16.7 ± 0.9	0.9 ± 0.4	29.2 ± 1.1	322.0 ± 2.7	467.0 ± 1.3	3880.0 ± 9.3	12.3 ± 2.5
RU Lup	1.5	0.6 ± 0.0	10.6 ± 0.1	0.5 ± 0.0	20.5 ± 0.2	2.3 ± 0.1	1.5 ± 0.1	8.8 ± 0.6	20.0 ± 1.0	2.0 ± 0.5	26.9 ± 1.1	319.0 ± 3.1	582.0 ± 1.6	4900.0 ± 12.0	6.3 ± 1.3
RU Lup	1.6	0.6 ± 0.0	7.2 ± 0.1	0.5 ± 0.0	12.9 ± 0.2	1.7 ± 0.1	1.3 ± 0.1	6.5 ± 0.6	15.7 ± 0.8	0.6 ± 0.4	33.6 ± 1.3	295.0 ± 2.6	529.0 ± 1.5	4760.0 ± 12.1	15.0 ± 3.0
RU Lup	1.7	0.7 ± 0.0	6.6 ± 0.1	0.4 ± 0.0	11.9 ± 0.2	1.6 ± 0.1	1.2 ± 0.1	4.8 ± 0.6	13.0 ± 0.9	1.7 ± 0.4	29.1 ± 1.1	308.0 ± 2.7	435.0 ± 1.3	4290.0 ± 10.9	1.4 ± 0.3
RU Lup	1.8	0.5 ± 0.0	7.0 ± 0.1	0.5 ± 0.0	12.9 ± 0.2	1.6 ± 0.1	1.4 ± 0.1	2.2 ± 0.5	17.0 ± 0.9	0.7 ± 0.5	37.8 ± 1.4	359.0 ± 3.2	558.0 ± 1.7	5360.0 ± 13.5	3.5 ± 0.7
RU Lup	1.9	0.6 ± 0.0	7.6 ± 0.1	0.5 ± 0.0	14.0 ± 0.2	1.5 ± 0.1	1.2 ± 0.1	6.0 ± 0.6	17.2 ± 0.9	1.3 ± 0.5	29.4 ± 1.2	297.0 ± 3.1	545.0 ± 1.5	5330.0 ± 13.8	10.3 ± 2.1
RU Lup	1.10	0.5 ± 0.0	9.5 ± 0.1	0.5 ± 0.0	19.0 ± 0.2	2.0 ± 0.1	1.5 ± 0.1	3.0 ± 0.6	19.7 ± 0.9	2.6 ± 0.5	24.4 ± 1.2	430.0 ± 3.5	574.0 ± 1.6	5320.0 ± 13.4	4.8 ± 1.0
RU Lup	2.1	0.8 ± 0.0	8.0 ± 0.1	0.5 ± 0.0	22.4 ± 0.3	3.2 ± 0.1	1.6 ± 0.1	5.0 ± 0.6	13.9 ± 0.7	1.5 ± 0.4	20.7 ± 0.9	263.0 ± 2.1	492.0 ± 1.3	3440.0 ± 8.9	11.3 ± 2.3
RU Lup	2.2	0.7 ± 0.0	5.1 ± 0.1	0.4 ± 0.0	13.3 ± 0.2	2.7 ± 0.1	0.8 ± 0.1	5.5 ± 0.6	9.6 ± 0.6	2.5 ± 0.4	16.9 ± 0.8	257.0 ± 2.7	284.0 ± 0.7	2180.0 ± 5.5	9.1 ± 1.8
RU Lup	2.3	0.5 ± 0.0	5.3 ± 0.1	0.4 ± 0.0	13.6 ± 0.2	2.4 ± 0.1	0.9 ± 0.1	4.6 ± 0.6	10.7 ± 0.6	1.4 ± 0.4	17.3 ± 1.0	326.0 ± 2.5	372.0 ± 1.0	2940.0 ± 7.5	7.5 ± 1.5
RU Lup	2.4	0.6 ± 0.0	5.6 ± 0.1	0.5 ± 0.0	15.8 ± 0.2	3.0 ± 0.1	1.2 ± 0.1	2.5 ± 0.4	9.3 ± 0.7	1.6 ± 0.3	15.0 ± 0.8	262.0 ± 2.4	272.0 ± 0.7	1930.0 ± 4.8	6.3 ± 1.3
RU Lup	2.5	0.7 ± 0.0	4.2 ± 0.1	0.5 ± 0.0	12.2 ± 0.2	2.8 ± 0.1	0.8 ± 0.1	3.7 ± 0.4	6.2 ± 0.4	1.7 ± 0.3	10.1 ± 0.7	242.0 ± 2.4	186.0 ± 0.5	1180.0 ± 3.0	5.0 ± 1.0
RU Lup	2.6	0.7 ± 0.0	3.5 ± 0.1	0.5 ± 0.0	10.4 ± 0.1	2.2 ± 0.1	0.7 ± 0.1	3.2 ± 0.4	6.0 ± 0.4	1.9 ± 0.3	11.5 ± 0.5	229.0 ± 2.4	186.0 ± 0.5	1220.0 ± 3.0	10.6 ± 2.1
RU Lup	2.7	0.7 ± 0.0	4.1 ± 0.1	0.5 ± 0.0	12.6 ± 0.2	2.3 ± 0.1	0.7 ± 0.1	4.9 ± 0.5	7.7 ± 0.6	2.6 ± 0.4	16.4 ± 0.6	233.0 ± 2.8	230.0 ± 0.6	1620.0 ± 4.1	6.3 ± 1.3
RU Lup	2.8	0.6 ± 0.0	3.6 ± 0.1	0.4 ± 0.0	11.2 ± 0.2	2.4 ± 0.1	0.9 ± 0.1	4.4 ± 0.5	5.5 ± 0.6	2.4 ± 0.3	15.4 ± 0.9	193.0 ± 2.1	243.0 ± 0.6	1680.0 ± 4.4	8.9 ± 1.8
RU Lup	2.9	0.8 ± 0.0	3.7 ± 0.1	0.5 ± 0.0	12.2 ± 0.2	2.4 ± 0.1	0.9 ± 0.1	3.9 ± 0.4	6.6 ± 0.5	1.8 ± 0.3	10.2 ± 0.6	191.0 ± 2.2	202.0 ± 0.5	1480.0 ± 3.8	12.6 ± 2.5
RU Lup	2.10	0.6 ± 0.0	3.1 ± 0.1	0.4 ± 0.0	8.8 ± 0.1	1.9 ± 0.1	0.7 ± 0.1	1.2 ± 0.5	6.6 ± 0.7	2.6 ± 0.5	14.9 ± 0.9	213.0 ± 2.7	330.0 ± 0.9	3110.0 ± 7.9	6.7 ± 1.3
RU Lup	2.11	0.5 ± 0.0	6.3 ± 0.1	0.5 ± 0.0	15.8 ± 0.2	2.2 ± 0.1	1.5 ± 0.1	1.4 ± 0.5	16.5 ± 0.8	1.9 ± 0.5	21.1 ± 1.1	242.0 ± 2.6	496.0 ± 1.4	3810.0 ± 9.6	3.8 ± 0.8
RU Lup	2.12	0.7 ± 0.0	7.5 ± 0.1	0.5 ± 0.0	16.8 ± 0.2	2.2 ± 0.1	1.5 ± 0.1	4.9 ± 0.7	15.5 ± 0.8	1.4 ± 0.5	22.4 ± 1.0	252.0 ± 2.8	528.0 ± 1.5	4170.0 ± 10.8	7.2 ± 1.5

Table 8
Same as Table 6, but for BP Tau

Object	Visit	Si III	Si IV	C I	C IV	He II	O III	Si II	Si III]	C III]	Al III]	Mg II	FUV	NUV	Bump
BP Tau	1.1	0.2 ± 0.0	1.0 ± 0.1	0.3 ± 0.1	8.1 ± 0.2	4.7 ± 0.3	0.6 ± 0.1	1.2 ± 0.2	2.0 ± 0.2	0.2 ± 0.2	0.9 ± 0.2	75.2 ± 0.5	386.0 ± 0.9	543.0 ± 1.3	69.5 ± 7.0
BP Tau	1.2	0.1 ± 0.0	1.1 ± 0.1	0.2 ± 0.0	10.4 ± 0.2	5.2 ± 0.3	0.3 ± 0.1	2.5 ± 0.1	1.9 ± 0.2	0.8 ± 0.1	1.3 ± 0.1	80.9 ± 0.6	133.0 ± 0.3	344.0 ± 0.9	24.8 ± 2.5
BP Tau	1.3	0.3 ± 0.1	1.4 ± 0.1	0.2 ± 0.1	14.6 ± 0.2	6.2 ± 0.2	0.8 ± 0.1	2.1 ± 0.2	2.4 ± 0.2	0.4 ± 0.2	0.5 ± 0.2	66.6 ± 0.5	347.0 ± 0.8	575.0 ± 1.4	34.5 ± 3.5
BP Tau	1.4	0.3 ± 0.0	0.6 ± 0.0	0.2 ± 0.0	6.4 ± 0.2	4.0 ± 0.2	0.3 ± 0.1	0.9 ± 0.2	1.8 ± 0.2	−0.0 ± 0.1	0.3 ± 0.2	42.3 ± 0.4	199.0 ± 0.5	340.0 ± 0.8	48.2 ± 4.9
BP Tau	1.5	0.1 ± 0.0	1.6 ± 0.1	0.2 ± 0.0	14.3 ± 0.2	3.4 ± 0.2	0.6 ± 0.1	2.0 ± 0.2	3.5 ± 0.2	0.8 ± 0.1	1.3 ± 0.2	84.5 ± 0.7	242.0 ± 0.6	471.0 ± 1.2	35.3 ± 3.6
BP Tau	1.6	0.2 ± 0.0	0.8 ± 0.0	0.2 ± 0.0	8.5 ± 0.2	4.1 ± 0.2	0.4 ± 0.1	1.4 ± 0.1	1.5 ± 0.2	0.9 ± 0.1	1.0 ± 0.1	65.6 ± 0.6	115.0 ± 0.3	327.0 ± 0.8	5.2 ± 0.6
BP Tau	1.7	0.1 ± 0.0	1.1 ± 0.1	0.2 ± 0.0	10.5 ± 0.2	4.9 ± 0.2	0.6 ± 0.1	2.2 ± 0.1	1.2 ± 0.1	0.5 ± 0.1	0.8 ± 0.1	59.1 ± 0.5	160.0 ± 0.4	394.0 ± 1.0	28.8 ± 3.0
BP Tau	1.8	0.2 ± 0.0	0.9 ± 0.1	0.2 ± 0.0	8.4 ± 0.2	4.5 ± 0.2	0.9 ± 0.1	1.6 ± 0.1	1.2 ± 0.2	0.1 ± 0.1	0.9 ± 0.2	71.9 ± 0.5	178.0 ± 0.4	381.0 ± 1.0	38.7 ± 3.9
BP Tau	1.9	0.2 ± 0.0	0.7 ± 0.1	0.2 ± 0.0	8.1 ± 0.2	4.7 ± 0.2	0.6 ± 0.1	1.9 ± 0.2	1.9 ± 0.2	0.2 ± 0.1	0.9 ± 0.2	58.1 ± 0.5	301.0 ± 0.7	399.0 ± 1.0	77.4 ± 7.8
BP Tau	1.10	0.2 ± 0.0	0.6 ± 0.0	0.2 ± 0.0	7.5 ± 0.2	4.2 ± 0.2	0.4 ± 0.1	0.5 ± 0.1	1.1 ± 0.2	0.4 ± 0.1	0.4 ± 0.2	49.7 ± 0.5	158.0 ± 0.4	356.0 ± 0.9	11.8 ± 1.2
BP Tau	1.11	0.3 ± 0.0	0.9 ± 0.1	0.2 ± 0.0	8.6 ± 0.2	5.3 ± 0.2	0.6 ± 0.1	1.6 ± 0.1	1.6 ± 0.2	0.4 ± 0.1	1.1 ± 0.2	52.0 ± 0.5	154.0 ± 0.4	356.0 ± 0.9	13.6 ± 1.4
BP Tau	1.12	0.3 ± 0.0	0.6 ± 0.0	0.2 ± 0.0	6.2 ± 0.2	3.6 ± 0.2	0.2 ± 0.1	1.3 ± 0.1	1.0 ± 0.1	0.4 ± 0.1	0.7 ± 0.1	44.9 ± 0.4	84.8 ± 0.2	241.0 ± 0.6	30.2 ± 3.1
BP Tau	2.1	0.1 ± 0.0	1.0 ± 0.0	0.1 ± 0.0	6.9 ± 0.1	4.9 ± 0.2	0.4 ± 0.1	0.7 ± 0.2	1.6 ± 0.3	0.6 ± 0.2	1.7 ± 0.3	72.6 ± 0.8	112.0 ± 0.3	313.0 ± 0.8	5.0 ± 0.6
BP Tau	2.2	0.2 ± 0.0	1.1 ± 0.1	0.2 ± 0.0	7.2 ± 0.2	4.3 ± 0.2	0.5 ± 0.1	1.4 ± 0.2	1.5 ± 0.2	0.7 ± 0.2	0.9 ± 0.3	54.5 ± 0.7	140.0 ± 0.3	355.0 ± 0.9	15.6 ± 1.6
BP Tau	2.3	0.2 ± 0.0	0.9 ± 0.0	0.1 ± 0.0	6.2 ± 0.1	3.7 ± 0.2	0.3 ± 0.1	0.6 ± 0.2	0.7 ± 0.2	0.5 ± 0.2	1.2 ± 0.2	57.3 ± 0.8	71.2 ± 0.2	240.0 ± 0.6	4.3 ± 0.5
BP Tau	2.4	0.3 ± 0.0	2.3 ± 0.1	0.2 ± 0.0	16.0 ± 0.3	7.6 ± 0.2	0.5 ± 0.1	0.4 ± 0.2	0.9 ± 0.2	0.7 ± 0.2	1.0 ± 0.2	35.2 ± 0.6	155.0 ± 0.4	359.0 ± 0.9	14.4 ± 1.5
BP Tau	2.5	0.1 ± 0.0	0.9 ± 0.1	0.1 ± 0.0	7.6 ± 0.1	6.4 ± 0.2	0.4 ± 0.1	1.4 ± 0.3	0.7 ± 0.3	−0.4 ± 0.3	0.4 ± 0.2	55.0 ± 0.9	192.0 ± 0.4	300.0 ± 0.9	15.4 ± 1.6
BP Tau	2.6	0.1 ± 0.0	1.0 ± 0.0	0.1 ± 0.0	7.6 ± 0.2	6.2 ± 0.2	0.3 ± 0.1	1.2 ± 0.2	0.7 ± 0.2	0.3 ± 0.1	1.2 ± 0.2	42.8 ± 0.7	81.1 ± 0.2	303.0 ± 0.7	5.9 ± 0.7
BP Tau	2.7	0.1 ± 0.0	0.7 ± 0.0	0.1 ± 0.0	5.5 ± 0.1	4.5 ± 0.2	0.2 ± 0.1	0.9 ± 0.2	0.6 ± 0.3	−0.3 ± 0.2	1.1 ± 0.2	36.5 ± 0.6	94.1 ± 0.2	264.0 ± 0.7	7.0 ± 0.7
BP Tau	2.8	0.1 ± 0.0	0.6 ± 0.0	0.1 ± 0.0	5.9 ± 0.1	4.7 ± 0.2	0.3 ± 0.1	0.3 ± 0.2	0.4 ± 0.2	−0.3 ± 0.2	1.0 ± 0.2	43.5 ± 0.7	117.0 ± 0.3	343.0 ± 0.9	20.5 ± 2.1
BP Tau	2.9	0.1 ± 0.0	1.2 ± 0.1	0.2 ± 0.0	9.1 ± 0.2	7.3 ± 0.2	0.4 ± 0.1	0.8 ± 0.3	1.2 ± 0.3	0.2 ± 0.3	1.1 ± 0.3	58.1 ± 0.8	217.0 ± 0.5	491.0 ± 1.2	26.4 ± 2.7
BP Tau	2.10	0.2 ± 0.0	1.1 ± 0.0	0.1 ± 0.0	7.5 ± 0.1	4.8 ± 0.2	0.3 ± 0.1	1.3 ± 0.2	0.5 ± 0.2	0.2 ± 0.2	1.1 ± 0.2	52.2 ± 0.9	101.0 ± 0.2	299.0 ± 0.7	17.8 ± 1.8
BP Tau	2.11	0.2 ± 0.0	1.1 ± 0.0	0.2 ± 0.0	7.3 ± 0.1	5.2 ± 0.2	0.6 ± 0.1	0.7 ± 0.2	0.6 ± 0.2	0.4 ± 0.2	1.2 ± 0.2	50.1 ± 0.8	148.0 ± 0.4	357.0 ± 0.9	21.2 ± 2.2
BP Tau	2.12	0.2 ± 0.0	1.1 ± 0.0	0.1 ± 0.0	8.4 ± 0.1	5.2 ± 0.2	0.4 ± 0.1	1.5 ± 0.3	1.3 ± 0.3	0.1 ± 0.2	1.6 ± 0.3	81.4 ± 0.9	157.0 ± 0.4	437.0 ± 1.1	8.2 ± 0.8

Table 9
Same as Table 6, but for GM Aur

Object	Visit	Si III	Si IV	C I	C IV	He II	O III	Si II	Si III]	C III]	Al III]	Mg II	FUV	NUV	Bump
GM Aur	1.1	0.4 ± 0.0	0.4 ± 0.0	0.3 ± 0.0	5.3 ± 0.1	1.9 ± 0.1	0.1 ± 0.1	0.2 ± 0.1	0.1 ± 0.1	0.0 ± 0.1	0.6 ± 0.1	24.0 ± 0.3	52.7 ± 0.1	161.0 ± 0.4	22.4 ± 2.3
GM Aur	1.2	0.4 ± 0.0	0.5 ± 0.0	0.3 ± 0.0	6.3 ± 0.1	2.7 ± 0.2	0.2 ± 0.1	0.0 ± 0.1	0.2 ± 0.1	0.4 ± 0.1	0.1 ± 0.1	23.5 ± 0.4	150.0 ± 0.4	343.0 ± 0.9	11.7 ± 1.3
GM Aur	1.3	0.5 ± 0.0	0.4 ± 0.0	0.3 ± 0.0	4.4 ± 0.1	1.8 ± 0.1	0.1 ± 0.1	0.3 ± 0.1	0.1 ± 0.1	0.1 ± 0.1	0.3 ± 0.1	20.0 ± 0.3	76.9 ± 0.2	179.0 ± 0.4	32.2 ± 3.3
GM Aur	1.4	0.4 ± 0.0	0.4 ± 0.0	0.3 ± 0.0	3.1 ± 0.1	1.3 ± 0.2	0.0 ± 0.1	0.2 ± 0.1	0.0 ± 0.1	0.1 ± 0.1	0.6 ± 0.1	23.9 ± 0.3	46.2 ± 0.1	157.0 ± 0.4	23.5 ± 2.4
GM Aur	1.5	0.4 ± 0.0	0.5 ± 0.0	0.3 ± 0.0	6.3 ± 0.1	2.0 ± 0.1	0.0 ± 0.1	0.3 ± 0.1	0.2 ± 0.1	0.1 ± 0.1	0.5 ± 0.1	26.3 ± 0.3	67.2 ± 0.2	236.0 ± 0.6	22.7 ± 2.4
GM Aur	1.6	0.4 ± 0.0	0.6 ± 0.0	0.3 ± 0.0	11.8 ± 0.2	3.1 ± 0.1	0.0 ± 0.1	0.6 ± 0.1	0.3 ± 0.1	0.1 ± 0.1	0.6 ± 0.1	41.5 ± 0.4	157.0 ± 0.4	487.0 ± 1.2	37.2 ± 3.8
GM Aur	1.7	0.3 ± 0.0	0.8 ± 0.0	0.4 ± 0.0	12.4 ± 0.2	3.3 ± 0.2	0.7 ± 0.1	0.4 ± 0.1	0.7 ± 0.1	0.2 ± 0.1	0.0 ± 0.2	39.3 ± 0.4	393.0 ± 0.9	737.0 ± 1.9	58.9 ± 6.1
GM Aur	1.8	0.4 ± 0.0	0.4 ± 0.0	0.3 ± 0.0	4.0 ± 0.1	1.7 ± 0.1	0.1 ± 0.1	0.2 ± 0.1	0.1 ± 0.1	0.1 ± 0.1	0.2 ± 0.2	14.4 ± 0.5	44.8 ± 0.1	132.0 ± 0.3	26.5 ± 2.7
GM Aur	1.9	0.4 ± 0.0	0.5 ± 0.0	0.3 ± 0.0	7.3 ± 0.2	2.7 ± 0.1	0.1 ± 0.1	0.1 ± 0.2	0.3 ± 0.1	0.2 ± 0.2	0.1 ± 0.3	19.0 ± 0.6	148.0 ± 0.4	360.0 ± 0.9	47.0 ± 4.8
GM Aur	1.10	0.3 ± 0.0	0.4 ± 0.0	0.3 ± 0.0	5.2 ± 0.1	1.8 ± 0.1	0.1 ± 0.1	0.6 ± 0.2	0.0 ± 0.1	0.1 ± 0.1	0.6 ± 0.2	17.7 ± 0.5	60.0 ± 0.1	191.0 ± 0.5	35.6 ± 3.6
GM Aur	1.11	0.3 ± 0.0	0.3 ± 0.0	0.2 ± 0.0	2.6 ± 0.1	1.0 ± 0.1	0.1 ± 0.1	0.2 ± 0.2	0.3 ± 0.1	0.3 ± 0.1	0.2 ± 0.2	13.9 ± 0.5	59.1 ± 0.1	156.0 ± 0.4	28.8 ± 2.9
GM Aur	2.1	0.3 ± 0.0	0.3 ± 0.0	0.2 ± 0.0	4.8 ± 0.1	2.0 ± 0.1	0.2 ± 0.1	0.1 ± 0.1	0.1 ± 0.1	0.1 ± 0.1	0.1 ± 0.1	19.0 ± 0.2	46.2 ± 0.1	149.0 ± 0.4	30.5 ± 3.1
GM Aur	2.2	0.4 ± 0.0	0.3 ± 0.0	0.3 ± 0.0	5.0 ± 0.1	2.3 ± 0.1	0.1 ± 0.1	0.2 ± 0.1	0.1 ± 0.1	0.1 ± 0.1	0.2 ± 0.1	19.5 ± 0.3	59.0 ± 0.1	187.0 ± 0.5	30.3 ± 3.1
GM Aur	2.3	0.4 ± 0.0	0.5 ± 0.0	0.2 ± 0.0	5.9 ± 0.2	2.3 ± 0.2	0.2 ± 0.1	0.4 ± 0.2	0.6 ± 0.1	0.1 ± 0.1	−0.1 ± 0.1	24.5 ± 0.4	280.0 ± 0.7	449.0 ± 1.2	29.2 ± 3.0
GM Aur	2.4	0.3 ± 0.0	0.4 ± 0.0	0.2 ± 0.0	5.9 ± 0.2	1.9 ± 0.1	0.1 ± 0.1	0.2 ± 0.1	0.2 ± 0.1	0.1 ± 0.1	0.2 ± 0.1	19.5 ± 0.3	60.0 ± 0.1	201.0 ± 0.5	31.1 ± 3.2
GM Aur	2.5	0.3 ± 0.0	0.4 ± 0.0	0.2 ± 0.0	5.0 ± 0.1	1.7 ± 0.2	0.2 ± 0.1	0.3 ± 0.1	0.1 ± 0.1	0.0 ± 0.1	−0.0 ± 0.1	22.2 ± 0.4	83.2 ± 0.2	246.0 ± 0.7	31.1 ± 3.2
GM Aur	2.6	0.3 ± 0.0	0.4 ± 0.0	0.2 ± 0.0	6.2 ± 0.1	2.2 ± 0.2	0.2 ± 0.1	0.2 ± 0.1	−0.0 ± 0.1	0.1 ± 0.1	0.4 ± 0.1	29.4 ± 0.4	75.9 ± 0.2	288.0 ± 0.7	20.0 ± 2.1
GM Aur	2.7	0.3 ± 0.0	0.4 ± 0.0	0.2 ± 0.0	5.1 ± 0.1	2.3 ± 0.2	0.3 ± 0.1	0.1 ± 0.1	0.2 ± 0.1	0.2 ± 0.1	0.3 ± 0.1	22.4 ± 0.3	100.0 ± 0.2	280.0 ± 0.7	24.6 ± 2.6
GM Aur	2.8	0.3 ± 0.0	0.3 ± 0.0	0.2 ± 0.0	5.0 ± 0.1	1.6 ± 0.1	0.1 ± 0.1	0.3 ± 0.1	0.1 ± 0.1	0.3 ± 0.1	0.1 ± 0.1	17.8 ± 0.3	64.8 ± 0.2	194.0 ± 0.5	36.3 ± 3.7
GM Aur	2.9	0.3 ± 0.0	0.4 ± 0.0	0.2 ± 0.0	6.1 ± 0.1	2.3 ± 0.1	0.1 ± 0.1	0.1 ± 0.1	0.4 ± 0.1	0.1 ± 0.1	0.0 ± 0.1	20.9 ± 0.3	71.8 ± 0.2	205.0 ± 0.5	18.3 ± 1.9
GM Aur	2.10	0.4 ± 0.0	0.4 ± 0.0	0.2 ± 0.0	6.0 ± 0.1	3.4 ± 0.2	0.2 ± 0.1	0.2 ± 0.1	0.0 ± 0.1	0.1 ± 0.1	0.2 ± 0.1	23.9 ± 0.4	62.6 ± 0.2	258.0 ± 0.7	14.6 ± 1.5
GM Aur	2.11	0.3 ± 0.0	0.3 ± 0.0	0.2 ± 0.0	4.5 ± 0.1	2.0 ± 0.1	0.1 ± 0.1	0.3 ± 0.1	0.2 ± 0.1	0.2 ± 0.1	0.1 ± 0.1	22.5 ± 0.3	84.6 ± 0.2	262.0 ± 0.6	15.3 ± 1.6

Table 10
L_{acc}–L_{UV} Log–Log Linear Fit Coefficients

Line	Coefficient	TW Hya	RU Lup	BP Tau	GM Aur	Global
Mg II	m	$0.20^{0.10}_{0.10}$	$1.85^{0.08}_{0.07}$	$0.76^{0.10}_{0.10}$	$1.25^{0.07}_{0.07}$	$0.78^{0.01}_{0.01}$
Mg II	b	$-0.75^{0.27}_{0.26}$	$3.88^{0.16}_{0.16}$	$1.31^{0.29}_{0.30}$	$3.08^{0.24}_{0.22}$	$1.33^{0.02}_{0.02}$
Mg II	r	$0.10^{0.05}_{0.05}$	$0.73^{0.02}_{0.02}$	$0.59^{0.07}_{0.07}$	$0.75^{0.03}_{0.03}$	$0.66^{0.01}_{0.01}$
Mg II	p	$0.68^{0.15}_{0.14}$	$<0.01^{0.00}_{0.00}$	$<0.01^{0.01}_{0.00}$	$<0.01^{0.00}_{0.00}$	$<0.01^{0.00}_{0.00}$
Al III]	m	$0.02^{0.15}_{0.10}$	$1.14^{0.08}_{0.08}$	$0.02^{0.10}_{0.10}$	$-0.05^{0.08}_{0.05}$	$0.30^{0.07}_{0.07}$
Al III]	b	$-1.23^{0.64}_{0.46}$	$3.63^{0.26}_{0.25}$	$-0.78^{0.47}_{0.45}$	$-1.22^{0.43}_{0.27}$	$0.51^{0.27}_{0.27}$
Al III]	r	$0.04^{0.29}_{0.25}$	$0.87^{0.03}_{0.03}$	$0.04^{0.20}_{0.21}$	$-0.24^{0.41}_{0.26}$	$0.55^{0.06}_{0.07}$
Al III]	p	$0.44^{0.36}_{0.30}$	$<0.01^{0.00}_{0.00}$	$0.51^{0.34}_{0.32}$	$0.20^{0.49}_{0.17}$	$<0.01^{0.00}_{0.00}$
C III]	m	$0.03^{0.09}_{0.07}$	$-0.10^{0.07}_{0.08}$	$2.5e\text{-}3^{0.03}_{0.03}$	$0.01^{0.05}_{0.04}$	$0.08^{0.04}_{0.03}$
C III]	b	$-1.16^{0.40}_{0.33}$	$-0.52^{0.32}_{0.34}$	$-0.83^{0.16}_{0.14}$	$-0.90^{0.25}_{0.23}$	$-0.37^{0.20}_{0.17}$
C III]	r	$0.06^{0.15}_{0.15}$	$-0.21^{0.16}_{0.14}$	$0.01^{0.16}_{0.16}$	$0.06^{0.20}_{0.21}$	$0.15^{0.07}_{0.06}$
C III]	p	$0.63^{0.24}_{0.33}$	$0.35^{0.38}_{0.23}$	$0.64^{0.26}_{0.27}$	$0.51^{0.34}_{0.33}$	$0.16^{0.24}_{0.12}$
Si III]	m	$0.07^{0.11}_{0.09}$	$0.98^{0.10}_{0.09}$	$0.12^{0.07}_{0.05}$	$0.05^{0.05}_{0.04}$	$0.33^{0.06}_{0.06}$
Si III]	b	$-0.95^{0.48}_{0.42}$	$3.36^{0.33}_{0.30}$	$-0.32^{0.32}_{0.24}$	$-0.70^{0.27}_{0.22}$	$0.70^{0.26}_{0.25}$
Si III]	r	$0.15^{0.21}_{0.21}$	$0.88^{0.03}_{0.04}$	$0.29^{0.13}_{0.12}$	$0.25^{0.19}_{0.20}$	$0.61^{0.05}_{0.06}$
Si III]	p	$0.44^{0.37}_{0.34}$	$<0.01^{0.00}_{0.00}$	$0.16^{0.27}_{0.13}$	$0.27^{0.45}_{0.22}$	$<0.01^{0.00}_{0.00}$
Si II	m	$-0.02^{0.09}_{0.06}$	$0.09^{0.12}_{0.09}$	$0.12^{0.07}_{0.05}$	$0.01^{0.06}_{0.04}$	$0.24^{0.07}_{0.06}$
Si II	b	$-1.34^{0.40}_{0.28}$	$0.28^{0.47}_{0.37}$	$-0.28^{0.29}_{0.25}$	$-0.92^{0.33}_{0.23}$	$0.30^{0.32}_{0.26}$
Si II	r	$-0.05^{0.24}_{0.20}$	$0.12^{0.11}_{0.12}$	$0.30^{0.11}_{0.11}$	$0.03^{0.24}_{0.19}$	$0.38^{0.06}_{0.06}$
Si II	p	$0.50^{0.35}_{0.32}$	$0.59^{0.27}_{0.29}$	$0.16^{0.23}_{0.11}$	$0.53^{0.33}_{0.35}$	$<0.01^{0.00}_{0.00}$
O III]	m	$0.30^{0.25}_{0.26}$	$0.97^{0.20}_{0.17}$	$0.10^{0.08}_{0.09}$	$0.03^{0.04}_{0.03}$	$0.24^{0.08}_{0.07}$
O III]	b	$0.17^{1.21}_{1.24}$	$4.32^{0.94}_{0.77}$	$-0.37^{0.40}_{0.45}$	$-0.81^{0.21}_{0.18}$	$0.41^{0.37}_{0.33}$
O III]	r	$0.37^{0.22}_{0.29}$	$0.65^{0.09}_{0.11}$	$0.22^{0.18}_{0.21}$	$0.15^{0.17}_{0.17}$	$0.33^{0.06}_{0.06}$
O III]	p	$0.10^{0.61}_{0.09}$	$<0.01^{0.01}_{0.00}$	$0.29^{0.48}_{0.24}$	$0.47^{0.35}_{0.32}$	$<0.01^{0.01}_{0.00}$
He II	m	$1.76^{0.10}_{0.09}$	$-0.98^{0.20}_{0.21}$	$0.24^{0.17}_{0.15}$	$0.90^{0.15}_{0.14}$	$-0.54^{0.02}_{0.01}$
He II	b	$4.11^{0.31}_{0.28}$	$-4.24^{0.87}_{0.92}$	$0.09^{0.67}_{0.60}$	$2.87^{0.64}_{0.61}$	$-2.90^{0.06}_{0.05}$
He II	r	$0.85^{0.02}_{0.03}$	$-0.49^{0.10}_{0.08}$	$0.18^{0.11}_{0.11}$	$0.67^{0.06}_{0.07}$	$-0.56^{0.01}_{0.01}$
He II	p	$<0.01^{0.00}_{0.00}$	$0.02^{0.05}_{0.02}$	$0.41^{0.33}_{0.24}$	$<0.01^{0.00}_{0.00}$	$<0.01^{0.00}_{0.00}$
C IV	m	$1.40^{0.08}_{0.07}$	$1.16^{0.07}_{0.08}$	$0.62^{0.07}_{0.07}$	$1.03^{0.05}_{0.05}$	$-0.21^{0.01}_{0.01}$
C IV	b	$2.53^{0.20}_{0.19}$	$3.89^{0.25}_{0.28}$	$1.41^{0.25}_{0.24}$	$3.00^{0.20}_{0.20}$	$-1.52^{0.03}_{0.03}$
C IV	r	$0.86^{0.02}_{0.02}$	$0.51^{0.03}_{0.03}$	$0.55^{0.05}_{0.05}$	$0.81^{0.03}_{0.03}$	$-0.20^{0.01}_{0.01}$
C IV	p	$<0.01^{0.00}_{0.00}$	$0.02^{0.01}_{0.01}$	$<0.01^{0.01}_{0.00}$	$<0.01^{0.00}_{0.00}$	$0.07^{0.01}_{0.01}$
C I	m	$2.52^{0.55}_{0.51}$	$0.24^{0.56}_{0.52}$	$0.09^{0.11}_{0.13}$	$0.35^{0.23}_{0.21}$	$-0.27^{0.02}_{0.02}$
C I	b	$9.02^{2.21}_{2.10}$	$1.11^{2.74}_{2.57}$	$-0.34^{0.60}_{0.68}$	$0.84^{1.21}_{1.08}$	$-2.14^{0.11}_{0.11}$
C I	r	$0.50^{0.09}_{0.10}$	$0.08^{0.19}_{0.18}$	$0.16^{0.20}_{0.21}$	$0.25^{0.15}_{0.16}$	$-0.29^{0.02}_{0.02}$
C I	p	$0.02^{0.05}_{0.02}$	$0.53^{0.34}_{0.34}$	$0.39^{0.39}_{0.31}$	$0.26^{0.39}_{0.19}$	$<0.01^{0.00}_{0.00}$
Si IV	m	$2.73^{0.38}_{0.35}$	$1.18^{0.05}_{0.04}$	$0.39^{0.08}_{0.08}$	$0.99^{0.22}_{0.19}$	$0.30^{0.01}_{0.01}$
Si IV	b	$9.16^{1.45}_{1.32}$	$4.39^{0.17}_{0.16}$	$0.93^{0.38}_{0.35}$	$3.95^{1.08}_{0.95}$	$0.52^{0.04}_{0.03}$
Si IV	r	$0.57^{0.06}_{0.07}$	$0.84^{0.01}_{0.02}$	$0.43^{0.07}_{0.09}$	$0.61^{0.09}_{0.11}$	$0.33^{0.01}_{0.01}$
Si IV	p	$<0.01^{0.01}_{0.00}$	$<0.01^{0.00}_{0.00}$	$0.04^{0.07}_{0.03}$	$<0.01^{0.01}_{0.00}$	$<0.01^{0.00}_{0.00}$
Si III	m	$0.88^{0.48}_{0.47}$	$-0.79^{0.43}_{0.39}$	$-0.06^{0.10}_{0.09}$	$-0.13^{0.43}_{0.35}$	$-0.26^{0.02}_{0.02}$
Si III	b	$2.23^{1.93}_{1.87}$	$-3.88^{2.07}_{1.88}$	$-1.18^{0.54}_{0.48}$	$-1.62^{2.20}_{1.79}$	$-2.06^{0.10}_{0.11}$
Si III	r	$0.17^{0.09}_{0.09}$	$-0.27^{0.14}_{0.13}$	$-0.12^{0.20}_{0.18}$	$-0.08^{0.24}_{0.21}$	$-0.28^{0.02}_{0.02}$
Si III	p	$0.45^{0.28}_{0.20}$	$0.23^{0.34}_{0.16}$	$0.43^{0.37}_{0.29}$	$0.46^{0.37}_{0.31}$	$<0.01^{0.00}_{0.00}$
FUV	m	$0.88^{0.04}_{0.04}$	$1.26^{0.02}_{0.02}$	$0.40^{0.04}_{0.04}$	$0.68^{0.02}_{0.02}$	$1.23^{0.01}_{0.01}$
FUV	b	$0.95^{0.09}_{0.08}$	$2.44^{0.04}_{0.05}$	$0.10^{0.09}_{0.10}$	$0.86^{0.05}_{0.05}$	$2.15^{0.02}_{0.02}$
FUV	r	$0.92^{0.01}_{0.01}$	$0.98^{2.7e-3}_{2.9e-3}$	$0.55^{0.04}_{0.05}$	$0.88^{0.01}_{0.02}$	$0.85^{3.3e-3}_{3.3e-3}$
FUV	p	$<0.01^{0.00}_{0.00}$	$<0.01^{0.00}_{0.00}$	$<0.01^{0.01}_{0.00}$	$<0.01^{0.00}_{0.00}$	$<0.01^{0.00}_{0.00}$
NUV	m	$1.05^{0.04}_{0.04}$	$1.01^{0.02}_{0.02}$	$0.94^{0.08}_{0.09}$	$0.95^{0.03}_{0.03}$	$0.92^{0.01}_{0.01}$
NUV	b	$1.10^{0.09}_{0.09}$	$1.02^{0.02}_{0.02}$	$1.06^{0.17}_{0.18}$	$1.13^{0.06}_{0.06}$	$0.94^{0.01}_{0.01}$
NUV	r	$0.96^{0.01}_{0.01}$	$0.99^{1.9e-3}_{2.5e-3}$	$0.66^{0.05}_{0.05}$	$0.92^{0.01}_{0.01}$	$0.96^{2.1e-3}_{2.3e-3}$

Table 10
(Continued)

Line	Coefficient	TW Hya	RU Lup	BP Tau	GM Aur	Global
NUV	p	$<0.01^{0.00}_{0.00}$	$<0.01^{0.00}_{0.00}$	$<0.01^{0.00}_{0.00}$	$<0.01^{0.00}_{0.00}$	$<0.01^{0.00}_{0.00}$
H_2 bump	m	$0.99^{0.26}_{0.26}$	$-0.14^{0.10}_{0.10}$	$0.12^{0.03}_{0.03}$	$0.22^{0.12}_{0.12}$	$-0.13^{0.05}_{0.05}$
H_2 bump	b	$2.50^{0.99}_{0.99}$	$-0.63^{0.37}_{0.39}$	$-0.46^{0.11}_{0.10}$	$-0.28^{0.38}_{0.38}$	$-1.26^{0.19}_{0.19}$
H_2 bump	r	$0.54^{0.13}_{0.14}$	$-0.20^{0.13}_{0.14}$	$0.31^{0.08}_{0.08}$	$0.22^{0.11}_{0.12}$	$-0.11^{0.05}_{0.04}$
H_2 bump	p	$0.01^{0.06}_{0.01}$	$0.37^{0.36}_{0.25}$	$0.14^{0.15}_{0.08}$	$0.32^{0.33}_{0.19}$	$0.30^{0.24}_{0.16}$

Note. Fit takes the form of $\log_{10}(L_{acc}/L_{\odot}) = m \cdot \log_{10}(L_{UV}/L_{\odot}) + b$. Parameter r is the Pearson correlation coefficient, and p is the p-value of the null hypothesis. See Figure 3.

ORCID iDs

John Wendeborn https://orcid.org/0000-0002-6808-4066
Catherine C. Espaillat https://orcid.org/0000-0001-9227-5949
Sophia Lopez https://orcid.org/0009-0003-8647-672X
Thanawuth Thanathibodee https://orcid.org/0000-0003-4507-1710
Connor E. Robinson https://orcid.org/0000-0003-1639-510X
Caeley V. Pittman https://orcid.org/0000-0001-9301-6252
Nuria Calvet https://orcid.org/0000-0002-3950-5386
Nicole Flors https://orcid.org/0009-0002-0185-9098
Fredrick M. Walter https://orcid.org/0000-0001-7796-1756
Ágnes Kóspál https://orcid.org/0000-0001-7157-6275
Konstantin N. Grankin https://orcid.org/0000-0001-5707-8448
Ignacio Mendigutía https://orcid.org/0000-0002-0233-5328
Hans Moritz Günther https://orcid.org/0000-0003-4243-2840
Jochen Eislöffel https://orcid.org/0000-0001-6496-0252
Zhen Guo https://orcid.org/0000-0003-0292-4832
Kevin France https://orcid.org/0000-0002-1002-3674
Eleonora Fiorellino https://orcid.org/0000-0002-5261-6216
William J. Fischer https://orcid.org/0000-0002-3747-2496
Péter Ábrahám https://orcid.org/0000-0001-6015-646X
Gregory J. Herczeg https://orcid.org/0000-0002-7154-6065

References

Ádámkovics, M., Najita, J. R., & Glassgold, A. E. 2016, ApJ, 817, 82
Alcalá, J. M., Manara, C. F., Natta, A., et al. 2017, A&A, 600, A20
Alcalá, J. M., Natta, A., Manara, C. F., et al. 2014, A&A, 561, A2
Alencar, S. H. P., & Batalha, C. 2002, ApJ, 571, 378
Alencar, S. H. P., Bouvier, J., Walter, F. M., et al. 2012, A&A, 541, A116
Andrews, S. M., Huang, J., Pérez, L. M., et al. 2018, ApJL, 869, L41
Andrews, S. M., Wilner, D. J., Hughes, A. M., et al. 2012, ApJ, 744, 162
Andrews, S. M., Wilner, D. J., Zhu, Z., et al. 2016, ApJL, 820, L40
Ardila, D. R., Basri, G., Walter, F. M., Valenti, J. A., & Johns-Krull, C. M. 2002, ApJ, 567, 1013
Ardila, D. R., Herczeg, G. J., Gregory, S. G., et al. 2013, ApJS, 207, 1
Bae, J., Isella, A., Zhu, Z., et al. 2023, in ASP Conf. Ser. 534, Protostars and Planets VII, ed. S.-I. Inutsuka (San Francisco, CA: ASP)
Bergin, E., Calvet, N., Sitko, M. L., et al. 2004, ApJL, 614, L133
Bottorff, M. C., Ferland, G. J., & Straley, J. P. 2006, PASP, 118, 1176
Bouvier, J., Alencar, S. H. P., Harries, T. J., Johns-Krull, C. M., & Romanova, M. M. 2007, in Protostars and Planets V, ed. B. Reipurth, D. Jewitt, & K. Keil (Tucson, AZ: Univ. of Arizona Press), 479
Bouvier, J., Sousa, A., Pouilly, K., et al. 2023, A&A, 672, A5
Calvet, N., & Gullbring, E. 1998, ApJ, 509, 802
Calvet, N., Muzerolle, J., Briceño, C., et al. 2004, AJ, 128, 1294
Costigan, G., Vink, J. S., Scholz, A., Ray, T., & Testi, L. 2014, MNRAS, 440, 3444
Debes, J., Nealon, R., Alexander, R., et al. 2023, ApJ, 948, 36
Donati, J. F., Bouvier, J., Alencar, S. H., et al. 2020, MNRAS, 491, 5660
Donati, J. F., Gregory, S. G., Alencar, S. H. P., et al. 2011, MNRAS, 417, 472
Donati, J. F., Jardine, M. M., Gregory, S. G., et al. 2008, MNRAS, 386, 1234
Espaillat, C., Furlan, E., D'Alessio, P., et al. 2011, ApJ, 728, 49
Espaillat, C. C., Herczeg, G. J., Thanathibodee, T., et al. 2022, AJ, 163, 114
Espaillat, C. C., Robinson, C., Grant, S., & Reynolds, M. 2019, ApJ, 876, 121
Espaillat, C. C., Robinson, C. E., Romanova, M. M., et al. 2021, Natur, 597, 41
Evans, N. J. I., Dunham, I., Jørgensen, J. K., et al. 2009, ApJS, 181, 321
Fischer, W. J., Hillenbrand, L. A., Herczeg, G. J., et al. 2023, in ASP Conf. Ser. 534, Protostars and Planets VII, ed. S. Inutsuka et al. (San Francisco, CA: ASP), 355
Foreman-Mackey, D., Hogg, D. W., Lang, D., & Goodman, J. 2013, PASP, 125, 306
France, K., Arulanantham, N., Maloney, E., et al. 2023, AJ, 166, 67
France, K., Roueff, E., & Abgrall, H. 2017, ApJ, 844, 169
France, K., Schindhelm, R., Herczeg, G. J., et al. 2012, ApJ, 756, 171
Gahm, G. F., Walter, F. M., Stempels, H. C., Petrov, P. P., & Herczeg, G. J. 2008, A&A, 482, L35
Gaia Collaboration, Vallenari, A., Brown, A. G. A., et al. 2023, A&A, 674, A1
Gómez de Castro, A. I., & Franqueira, M. 1997, ApJ, 482, 465
Gorti, U., Dullemond, C. P., & Hollenbach, D. 2009, ApJ, 705, 1237
Grankin, K. N. 2016, AstL, 42, 314
Gravity Collaboration, Garcia Lopez, R., Natta, A., et al. 2020, Natur, 584, 547
GRAVITY Collaboration, Perraut, K., Labadie, L., et al. 2021, A&A, 655, A73
Gravity Collaboration, Wojtczak, J. A., Labadie, L., et al. 2023, A&A, 669, A59
Gullbring, E., Hartmann, L., Briceño, C., & Calvet, N. 1998, ApJ, 492, 323
Günther, H. M., Schmitt, J. H. M. M., Robrade, J., & Liefke, C. 2007, A&A, 466, 1111
Haffert, S. Y., Bohn, A. J., de Boer, J., et al. 2019, NatAs, 3, 749
Hartigan, P., Hartmann, L., Kenyon, S., Hewett, R., & Stauffer, J. 1989, ApJS, 70, 899
Hartmann, L., Herczeg, G., & Calvet, N. 2016, ARA&A, 54, 135
Herbst, W., Herbst, D. K., Grossman, E. J., & Weinstein, D. 1994, AJ, 108, 1906
Herczeg, G. J., Chen, Y., Donati, J.-F., et al. 2023, ApJ, 956, 102
Herczeg, G. J., & Hillenbrand, L. A. 2008, ApJ, 681, 594
Herczeg, G. J., Walter, F. M., Linsky, J. L., et al. 2005, AJ, 129, 2777
Herczeg, G. J., Wood, B. E., Linsky, J. L., Valenti, J. A., & Johns-Krull, C. M. 2004, ApJ, 607, 369
Hinton, P. C., France, K., Batista, M. G., et al. 2022, ApJ, 939, 82
Huang, J., Andrews, S. M., Cleeves, L. I., et al. 2018a, ApJ, 852, 122
Huang, J., Andrews, S. M., Dullemond, C. P., et al. 2018b, ApJL, 869, L42
Huang, J., Andrews, S. M., Dullemond, C. P., et al. 2020a, ApJ, 891, 48
Huang, J., Andrews, S. M., Öberg, K. I., et al. 2020b, ApJ, 898, 140
Huélamo, N., Figueira, P., Bonfils, X., et al. 2008, A&A, 489, L9
Ingleby, L., Calvet, N., Bergin, E., et al. 2009, ApJL, 703, L137
Ingleby, L., Calvet, N., Herczeg, G., & Briceño, C. 2012, ApJL, 752, L20
Ingleby, L., Calvet, N., Herczeg, G., et al. 2013, ApJ, 767, 112
Ingleby, L., Espaillat, C., Calvet, N., et al. 2015, ApJ, 805, 149
Jensen, E. L. N., & Mathieu, R. D. 1997, AJ, 114, 301
Johns-Krull, C. M. 2007, ApJ, 664, 975
Johns-Krull, C. M., Valenti, J. A., & Koresko, C. 1999, ApJ, 516, 900
Kastner, J. H., Huenemoerder, D. P., Schulz, N. S., Canizares, C. R., & Weintraub, D. A. 2002, ApJ, 567, 434
Keppler, M., Benisty, M., Müller, A., et al. 2018, A&A, 617, A44
Kulkarni, A. K., & Romanova, M. M. 2008, MNRAS, 386, 673
Long, F., Herczeg, G. J., Harsono, D., et al. 2019, ApJ, 882, 49

Long, M., Romanova, M. M., Kulkarni, A. K., & Donati, J. F. 2011, MNRAS, 413, 1061
Macías, E., Espaillat, C. C., Ribas, Á., et al. 2018, ApJ, 865, 37
Manara, C. F., Frasca, A., Venuti, L., et al. 2021, A&A, 650, A196
Manara, C. F., Testi, L., Natta, A., et al. 2014, A&A, 568, A18
McGinnis, P., Bouvier, J., & Gallet, F. 2020, MNRAS, 497, 2142
Miotello, A., Kamp, I., Birnstiel, T., Cleeves, L. C., & Kataoka, A. 2023, in ASP Conf. Ser. 534, Protostars and Planets VII, ed. S. Inutsuka et al. (San Francisco, CA: ASP), 501
Nayakshin, S., Tsukagoshi, T., Hall, C., et al. 2020, MNRAS, 495, 285
Osterloh, M., Thommes, E., & Kania, U. 1996, yCat, J/A+AS/120/267
Pascucci, I., Cabrit, S., Edwards, S., et al. 2023, in ASP Conf. Ser. 534, Protostars and Planets VII, ed. S. Inutsuka et al. (San Francisco, CA: ASP), 567
Percy, J. R., Esteves, S., Glasheen, J., et al. 2010, JAAVSO, 38, 151
Percy, J. R., Gryc, W. K., Wong, J. C. Y., & Herbst, W. 2006, PASP, 118, 1390
Percy, J. R., & Palaniappan, R. 2006, JAAVSO, 35, 290
Pérez, S., Casassus, S., Baruteau, C., et al. 2019, AJ, 158, 15
Pittman, C. V., Espaillat, C. C., Robinson, C. E., et al. 2022, AJ, 164, 201
Qi, C., Ho, P. T. P., Wilner, D. J., et al. 2004, ApJL, 616, L11
Ricker, G. R., Winn, J. N., Vanderspek, R., et al. 2015, JATIS, 1, 014003
Robinson, C. E., & Espaillat, C. C. 2019, ApJ, 874, 129
Roman-Duval, J., Proffitt, C. R., Taylor, J. M., et al. 2020, RNAAS, 4, 205
Romanova, M. M., Kulkarni, A. K., & Lovelace, R. V. E. 2008, ApJL, 673, L171
Romanova, M. M., Ustyugova, G. V., Koldoba, A. V., & Lovelace, R. V. E. 2012, MNRAS, 421, 63
Romanova, M. M., Ustyugova, G. V., Koldoba, A. V., Wick, J. V., & Lovelace, R. V. E. 2003, ApJ, 595, 1009
Schmitt, J. H. M. M., Robrade, J., Ness, J. U., Favata, F., & Stelzer, B. 2005, A&A, 432, L35
Sicilia-Aguilar, A., Campbell-White, J., Roccatagliata, V., et al. 2023, MNRAS, 526, 4885
Simon, T., Vrba, F. J., & Herbst, W. 1990, AJ, 100, 1957
Siwak, M., Ogloza, W., Moffat, A. F. J., et al. 2018, MNRAS, 478, 758
Siwak, M., Ogloza, W., Rucinski, S. M., et al. 2016, MNRAS, 456, 3972
Siwak, M., Rucinski, S. M., Matthews, J. M., et al. 2011, MNRAS, 410, 2725
Siwak, M., Rucinski, S. M., Matthews, J. M., et al. 2014, MNRAS, 444, 327
Sokal, K. R., Deen, C. P., Mace, G. N., et al. 2018, ApJ, 853, 120
Sousa, A. P., Bouvier, J., Alencar, S. H. P., et al. 2023, A&A, 670, A142
Stempels, H. C., Gahm, G. F., & Petrov, P. P. 2007, A&A, 461, 253
Stempels, H. C., & Piskunov, N. 2002, A&A, 391, 595
Stock, C., McGinnis, P., Caratti o Garatti, A., Natta, A., & Ray, T. P. 2022, A&A, 668, A94
Takami, M., Bailey, J., Gledhill, T. M., Chrysostomou, A., & Hough, J. H. 2001, MNRAS, 323, 177
Thanathibodee, T., Calvet, N., Herczeg, G., et al. 2018, ApJ, 861, 73
Venuti, L., Bouvier, J., Flaccomio, E., et al. 2014, A&A, 570, A82
Vrba, F. J., Rydgren, A. E., Chugainov, P. F., Shakovskaia, N. I., & Zak, D. S. 1986, ApJ, 306, 199
Whelan, E. T., Pascucci, I., Gorti, U., et al. 2021, ApJ, 913, 43
Whittet, D. C. B., Shenoy, S. S., Clayton, G. C., & Gordon, K. D. 2004, ApJ, 602, 291
Williams, J. P., & Cieza, L. A. 2011, ARA&A, 49, 67
Xu, Z., Herczeg, G. J., Johns-Krull, C. M., & France, K. 2021, ApJ, 921, 181
Yang, H., Herczeg, G. J., Linsky, J. L., et al. 2012, ApJ, 744, 121
Zhang, S., Kalscheur, M., Long, F., et al. 2023, ApJ, 952, 108
Zhou, Y., Sanghi, A., Bowler, B. P., et al. 2022, ApJL, 934, L13
Zhu, Z., Bailey, A., Macías, E., Muto, T., & Andrews, S. M. 2023, MNRAS, 518, 5808
Zhu, Z., Stone, J. M., & Calvet, N. 2024, MNRAS, 528, 2883
Zsidi, G., Manara, C. F., Kóspál, Á., et al. 2022, A&A, 660, A108